Wall-resolved Large Eddy Simulations of the transient turbulent fluid mixing in a closed system replicating a pressurized thermal shock

Pierre-Emmanuel Angeli

Flow, Turbulence and Combustion (2022) 108:43–75
https://doi.org/10.1007/s10494-021-00272-z

Wall-Resolved Large Eddy Simulations of the Transient Turbulent Fluid Mixing in a Closed System Replicating a Pressurized Thermal Shock

Pierre-Emmanuel Angeli[1]

Received: 6 October 2020 / Accepted: 10 May 2021 / Published online: 22 May 2021

Abstract
The isothermal mixing of a heavy and a light liquid of different physical properties is numerically investigated by means of Large Eddy Simulations. The validation is based on experimental data held in a system reproducing various components of a pressurized water nuclear reactor, during a scenario of cold water injection at a low Atwood number of 0.05. The flow has two distinct stages: first a buoyancy-driven phase is characterized by a fluid front development in the cold leg and gives rise to Kelvin–Helmholtz whorls under the action of density changes. Then, the heavy liquid discharges into the downcomer filled with light liquid, which causes a turbulent mixing. These phenomena are analyzed through a single-phase approach where the density of the working fluid is either variable or modeled by the Boussinesq approximation. The influence of grid refinement is deeply examined, which shows that the mesh convergence is well achieved for the main flow quantities, unlike the low-magnitude spanwise components. Overall, the numerical solutions are found to reproduce the experimental measurements with a fair accuracy for both physical models used. These latter exhibit similar trends, due to the small density difference under consideration. The predictions in the downcomer appear to be more challenging owing to a strongest turbulence than in the cold leg, some flow features being not properly captured. However, the experimental data in the downcomer are found to be incomplete and somewhat dubious for a strict validation of the numerical simulations. Lastly, the flow distribution in the dowcomer is investigated, providing further insight on the mixing process.

Keywords Large eddy simulation · Turbulent mixing · Variable density · Boussinesq approximation · TrioCFD · Pressurized thermal shock

List of Symbols

Latin Symbols

A	Atwood number
$(\mathscr{C})$, $(\mathscr{L})$	Circular and straight lines

✉ Pierre-Emmanuel Angeli
pierre-emmanuel.angeli@cea.fr

[1] CEA, Service de Thermo-hydraulique et de Mécanique des Fluides, Université Paris-Saclay, Gif-sur-Yvette 91191, France

$(\mathbf{e}_r\,;\mathbf{e}_\theta\,;\mathbf{e}_{z'})$	Cylindrical coordinate system
f	Time frequency
Fr	Froude number
$\boldsymbol{g}=(g_i)_{1\leq i\leq 3}$	Gravity field
$\mathscr{I}$	Time-averaging interval
$\mathscr{M}$	Mesh
$\mathcal{K}$	Turbulent kinetic energy
N	Number of experimental points
$\mathscr{N}$	Error norm
p, p^*	Pressure, modified pressure
$\mathcal{Q}_i^{\text{sgs}}$	Subgrid-scale mass flux vector
Ri	Richardson number
Sc, Sc_t	Schmidt, turbulent Schmidt numbers
t	Time
$\mathcal{T}_{ij}^{\text{sgs}}$	Subgrid-scale stress tensor
u_1, u, U	Horizontal velocity components
u_2, v, V	Vertical velocity components
u_3, w, W	Spanwise velocity components
$(U_r\,;U_\theta\,;U_{z'})$	Cylindrical velocity components
(x, y, z) or (x_1, x_2, x_3)	Space coordinates
Δx^+, Δy^+, Δz^+	Mesh size in wall units
y^+	Dimensionless wall distance

Greek Symbols

α_0	Coefficient of mass
δ_{ij}	Kronecker delta
θ	Azimuthal angle
μ	Dynamic viscosity
ρ	Density
σ_{ij}	Rate-of-strain tensor
ϕ	Mass fraction

Subscripts

0	Reference quantity
cl	Relative to cold leg
dc	Relative to downcomer
H	Relative to the heavy liquid
L	Relative to the light liquid
mean	Time-averaged
sd	Standard deviation
sgs	Subgrid-scale

Operators

$\widetilde{\cdot}$	Favre filter
$\bar{\cdot}$	Spatial filter

Abbreviations

BA	Boussinesq approximation

CLM	Cold leg mixing
FVE	Finite volume element
LES	Large eddy simulation
PTS	Pressurized thermal shock
PWR	Pressurized water reactor
RMSE	Root-mean-square error
SGS	SubGrid-scale
VD	Variable-density

1 Introduction

The turbulent mixing between two fluids of different properties occurs everywhere in the natural environment, but has also many industrial implications. Among them, it plays an essential role for safety issues in nuclear power plants, especially during the accidental scenario of loss-of-coolant in a Pressurized Water Reactor (PWR). During such an event, Emergency Core Cooling (ECC) water is injected through the cold leg into a plenum of warmer fluid, resulting in possible huge thermal stresses and pressure changes. This phenomenon called a Pressurized Thermal Shock (PTS) is likely to lead to a failure of the reactor vessel and consequently to a major accident. To avoid such an outcome, the accurate prediction of flow features and temperature stresses is essential. Experimental and numerical studies of turbulent fluid mixing are the subject of a plentiful literature and contribute to a better understanding of the phenomena at stake. The mixing of fluids of unequal densities produces hydrodynamics instabilities which are driven by the Atwood number, representing the density variation between the two fluids. The displacement flow caused by the injection of a heavy fluid into a light one in pipes with various inclination angles has been experimentally studied for the case where the fluids are newtonian and miscible (Akbari and Taghavi 2020; Taghavi et al. 2012a, b) or immiscible (Hasnain et al. 2017) at a wide range of Atwood numbers and for different cross-sections (Lefauve and Linden 2020). The influence of the dimensionless parameters involved in this process, among which the Reynolds, Froude and Archimede numbers, as well as the inclination angle of the pipe, have been investigated. Density and velocity statistics measurements in the resulting Rayleigh-Taylor and Kelvin-Helmholtz instabilities have been performed (Ramaprabhu and Andrews 2003), including high values of the Atwood number ($A > 0.6$) (Akula and Ranjan 2016).

With the increase in computational resources, Computational Fluid Dynamics (CFD) has become an increasingly used tool to simulate such kind of flow. Among the most recent works calling on CFD for the study of fluid mixing in the context of nuclear reactor safety, some authors have performed analyses using several turbulence models by comparison with experimental measurements in a test facility, in order to select suitable models *e.g.* for the calculation of boron dilution in PWR (Huang and Höhne 2019). In addition, the prediction of buoyancy-driven flows computed with Reynolds-Averaged Navier-Stokes (RANS) models including the radiation phenomenon (Kumara et al. 2020), and the simulation of buoyant plume and comparison of RANS predictions with experimental data in a simplified domain (Macpherson and Tunstall 2020), have been proposed. The PTS in pressurized nuclear reactors have been the subject of plentiful numerical studies employing various approaches, such as a coupling of multiple RANS models (standard k–ε, realizable k–ε and Reynolds-Stress models) (Hu et al. 2020), a two-phase CFD model including the effect of free-surface condensation (Cremer et al. 2019), a Direct Numerical Simulation (DNS) of

the flow and thermal fields with a discussion on the validity of the Boussinesq hypothesis (Shams et al. 2019). Moreover, the mixing process in nuclear reactor downcomers have been recently experimentally and numerically analyzed using RANS turbulence models (Eltayeb et al. 2021), or Large Eddy Simulation (LES) (Chouhan et al. 2021) with sensitivity to the coolant injection rate (Li et al. 2021). CFD is also used to evaluate the risk of crack initiation and propagation in a reactor pressure vessel (Uitslag-Doolaard et al. 2020; Ruan and Morishita 2021). A comprehensive review of the work carried out on the structural integrity of a reactor subjected to a PTS is done in Thamaraiselvi and Vishnuvardhan (2020).

The present study was accomplished within the framework of the OECD/NEA computational benchmark exercise "Cold Leg Mixing" (CLM) launched by the Working Group on the Analysis and Management of Accidents (WGAMA) (Herranz et al. 2020). It follows on from the previous benchmark GEMIX ("GEneric Mixing eXperiment") which also proposed a fluid mixing study but in a more academic configuration (Rakhimov et al. 2018). The CLM benchmark has been designed to perform Verification, Validation and Uncertainty Quantification (VVUQ) of CFD codes. The validation is made against experimental measurements provided by the Texas A&M University (Orea et al. 2020). The facility mimics the critical scenario of a PTS in a reactor vessel and the accurate prediction of the transient flow using CFD has been found to be a challenging issue. Some studies on this benchmark have already been published, using either LES (Lai et al. 2019, 2020) or RANS modeling (Hassan et al. 2021), and focusing on sensitivity analyses to input parameters such as the molecular and turbulent Schmidt numbers.

The CLM computations reported in the present paper are based on the in-house software TrioCFD (Angeli 2015), which was previously used in order to investigate various problems related to nuclear reactor safety, such as the boron dilution (Ducros et al. 2010) and the cold ECC water injection in a PWR vessel during a loss-of-coolant scenario (Bieder and Rodio 2019). It was also confronted with commercial codes on this type of issue (Höhne et al. 2018). TrioCFD includes a variable-density (or low-Mach number) model which has been first employed for the numerical study of a pebble bed reactor (Elmo and Cioni 2003). More recently, it was also successfully applied in several studies, from the DNS and LES of turbulent anisothermal channel flows (Aulery et al. 2017; Avellaneda et al. 2019; Dupuy et al. 2018, 2019) to validation of LES against hydrogen risk experimental measurements (Bernard-Michel et al. 2019; Saikali et al. 2019). The main objectives pursued by the present study are to capture a mesh-independent solution with fixed input parameters, investigate the influence of the variable density approach, gain information on the required mesh size for a reliable LES of this experiment, and complement the knowledge of the mixing process in the cold leg and in the downcomer. In the CLM exercise, the fluids are supposed to be miscible and the flow is treated in a single-phase point of view. Large Eddy Simulations are performed either with a uniform density resting on the Boussinesq approximation, or with a quasi-compressible model using a density depending of the concentration of the heavy fluid in the mixture. Various grid refinements allow to investigate the mesh convergence, and comparisons with first and second-order flow statistics are provided.

The paper is organized as follows. Section 2 describes the experimental facility Sect. 2.1 and the associated computational meshes Sect. 2.2. Section 3 describes the LES governing equations Sect. 3.1 and the numerical framework Sect. 3.3 employed in the simulations. Then, Sect. 4 proposes a mesh sensitivity study Sect. 4.1, a global flow analysis Sect. 4.2, a spectral analysis in downcomer Sect. 4.3 and comparisons of numerical solutions with experimental values in the cold leg Sect. 4.4 and in the downcomer Sect. 4.5. Additional

results about the velocity distribution in the annular space of the downcomer are given in Sect. 4.6, although no experimental data of this distribution exist. Finally, Sect. 5 concludes the article with a brief summary and a series of conclusions.

2 Experimental Facility and Computational Meshes

2.1 Experimental Facility

The experimental facility under consideration has been established by the Texas A&M University and consists of two vessels connected by a pipe, including a valve separating at the initial state a heavy fluid (a mixture of water and sodium chloride) and a light fluid (a mixture of water and ethanol) filling respectively the left and the right part of the domain, as shown in Fig. 1. The connection between the leg and the right tank shows a rounded design, as in a typical PWR vessel, but at a reduced scale of roughly 1:13. The whole fluid volume occupies a small part of a box of size $2.38 \times 0.61 \times 0.34$ m. When the valve is opened, the density gradient in the gravity field causes the heavy fluid to flow into the cold leg and to discharge into the "light" vessel. Simultaneously, an opposite flow of the light mixture develops in the cold leg and leads to the appearance of a plume in the "heavy" vessel.

The test facility replicates a cold water injection in a reactor pressure vessel, but the whole experiment takes place in isothermal conditions where the heavy and light fluids mimic the cold and hot water, respectively. The properties attached to the light and to the heavy liquid are respectively denoted by the indices "L" and "H". The Atwood number, defined as

$$\mathrm{A} = \frac{\rho_H - \rho_L}{\rho_H + \rho_L}, \tag{1}$$

is controlled by adjusting the compositions of the mixtures. Two sets of physical properties have been proposed in the benchmark, leading to Atwood numbers close to 0.05 in the open test, and 0.1 in the blind test. Only the smallest Atwood number is considered in the present article. The corresponding physical properties are gathered in Table 1.

The tank located on the right, i.e. the "light" vessel, is called the downcomer and has an annular volume formed by two concentric cylinders. The cold leg and the downcomer will be hereinafter referred to as "cl" and "dc". The initial time is taken at the moment when the valve opens. After a long time, the concentration field would reach a stationary stable stratified state with a fluid remaining at rest, but the experiment focuses on the transient state, which is observed over several tens of seconds. The measurement techniques are described in detail in Orea et al. (2020). The measurements are made by Particle Image Velocimetry (PIV) in two zones included in the plane $z = 0$, one in the cold leg and one in the downcomer. In each PIV plane represented on Fig. 2, the measuring points are uniformly distributed according to a Cartesian grid: there are respectively 1694 and 1207 points in the leg and downcomer measurement windows. These sets of points will be used later to compute Root-Mean-Square Errors (RMSE) between numerical solutions and measured values. As the flow is fully transient and turbulent, velocity statistics over several time averaging windows of 10 s are considered. Although this choice have been widely discussed (Lai et al. 2019), the first selected time intervals are $\mathscr{I}_{\mathrm{cl}} = [6.38\ \mathrm{s}\ ;\ 16.38\ \mathrm{s}]$ in the cold leg and $\mathscr{I}_{\mathrm{dc}} = [10.84\ \mathrm{s}\ ;\ 20.84\ \mathrm{s}]$ in the downcomer. The available experimental quantities are the

Fig. 1 Simplified drawings of the experimental facility: **a** 3D view of the whole closed system (CAD of the fluid volume), **b** cut plane at $y = 0$ and **c** cut plane at $z = 0$ (the red line ABCD is used later in the article, see Fig. 4)

average velocity $\boldsymbol{U}_{\text{mean}}$ and its standard deviation $\boldsymbol{U}_{\text{sd}}$. These data are computed using summations over a discrete series of N instantaneous velocity measurements and defined in the following way, with $k \in \{\text{cl;dc}\}$:

$$\boldsymbol{U}_{\text{mean}} = \frac{1}{N} \sum_{k \in \mathscr{I}_k} \boldsymbol{u}^{(k)}, \quad \boldsymbol{U}_{\text{sd}} = \sqrt{\frac{1}{N} \sum_{k \in \mathscr{I}_k} \left(\boldsymbol{u}^{(k)} - \boldsymbol{U}_{\text{mean}}\right)^2}. \tag{2}$$

The flow in spanwise direction is negligible in the cold leg, contrary to the downcomer owing to the diffusion of the heavy liquid in the annular gap of the downcomer. However, only the vertical and horizontal components of the previous velocity statistics are measured. The concentration field was not provided to the participants. Because of the computational costs, the physical times beyond 20.84 s are not handled in the present simulations.

2.2 Computational Meshes

The computational domain retained for the numerical simulations is the one represented on Fig. 1. Given the high aspect ratio between its total length and the pipe diameter, a large number of cells are necessary to fill the fluid volume. Moreover, the annular gap in the downcomer is less than 2 cm; consequently it requires the use of tiny cells in order to be correctly discretized. This geometric consideration is accentuated by the physical phenomena at stake, since the downcomer is the place where the strongest turbulence occurs. For these reasons, a local mesh refinement is carried out there. On the opposite side, the left tank being located far from the regions of interest, it is meshed in a coarser way than the rest of the domain. This choice is assumed to have little impact on the quality of solutions in the investigated zones and reduces somewhat the total number of mesh cells, saving significant computational cost. In order to examine the influence of mesh size on the numerical solutions, four tetrahedral meshes $\mathscr{M}_i$ with different refinement levels are constructed. They are numbered from $i = 1$ to 4, from the coarsest to the finest. The global mesh size is roughly divided by two between two consecutive meshes. The meshes are generated using the Octree algorithm of the ANSYS IcemCFD software. The simulations are wall-resolved and thereby require a careful meshing of the boundary layers for a correct representation of velocity and concentration gradients. For this purpose, several prism layers of various thickness and geometric progression factors are extruded along the walls and then divided into tetrahedra. This allows to easily control the near-wall tetraedra size and produces mesh faces normal to the mean flow direction at wall, yielding a better numerical accuracy. In the numerical discretization employed, the degrees of freedom (d.o.f.) are located at the center of faces for the velocity components and concentration, and both at the center of tetraedra and at nodes for the pressure field, as detailed in paragraph Sect. 3.3. An overview of the meshes as well as their main characteristics are provided in Fig. 3 and in Table 2.

As already pointed out, the resolution is made without any wall functions, because their use would introduce a wrong representation of the friction at wall, especially along the smooth nozzle and the downcomer walls, where the boundary layer is subjected to separation and recirculation. Figure 4 indicates the average and RMS values of y^+ along the boundary ABCD represented on Fig. 1c, obtained by Large Eddy Simulations with the

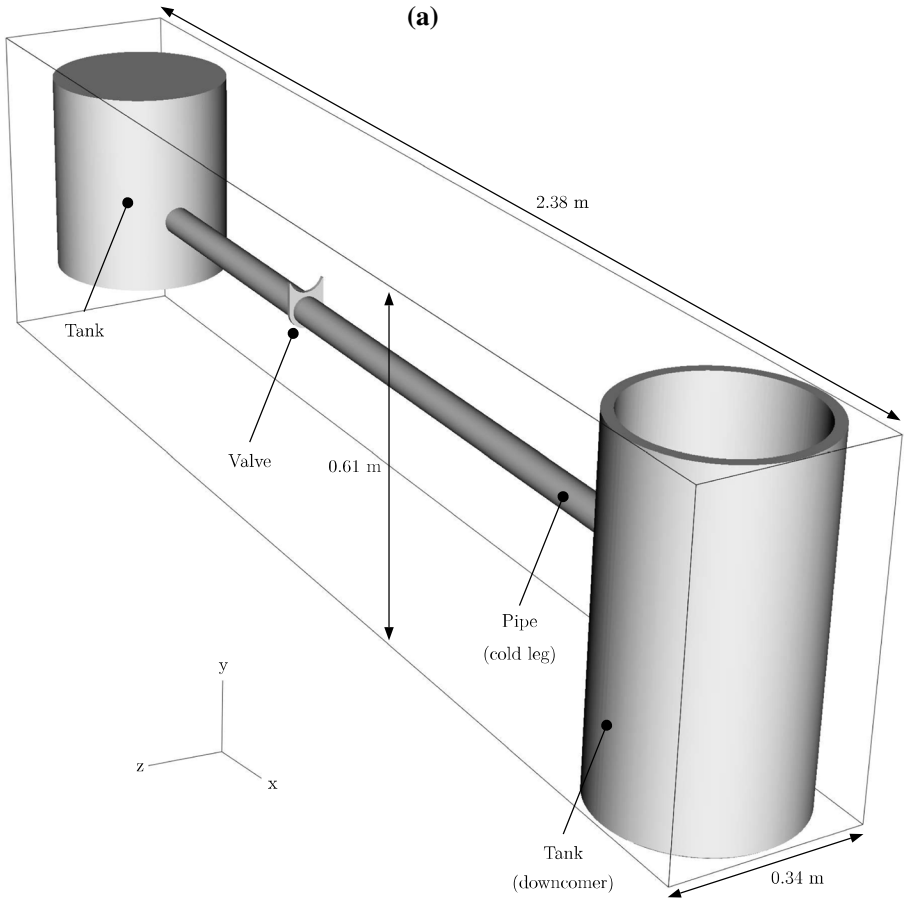
(a)
2.38 m
Tank
Valve
0.61 m
Pipe
(cold leg)
y
z
x
Tank
(downcomer)
0.34 m
(b)
Smooth nozzle
Valve
x
z
Volume filled with heavy liquid
Volume filled with light liquid
(c)
y
x
A
B
C
D

Table 1 Fluid properties for the smallest Atwood number

	Density (kg m^{-3})	Dynamic viscosity (Pa s)
Light liquid	956.54	0.00245
Heavy liquid	1064.70	0.00109
Average	1010.62	0.00177

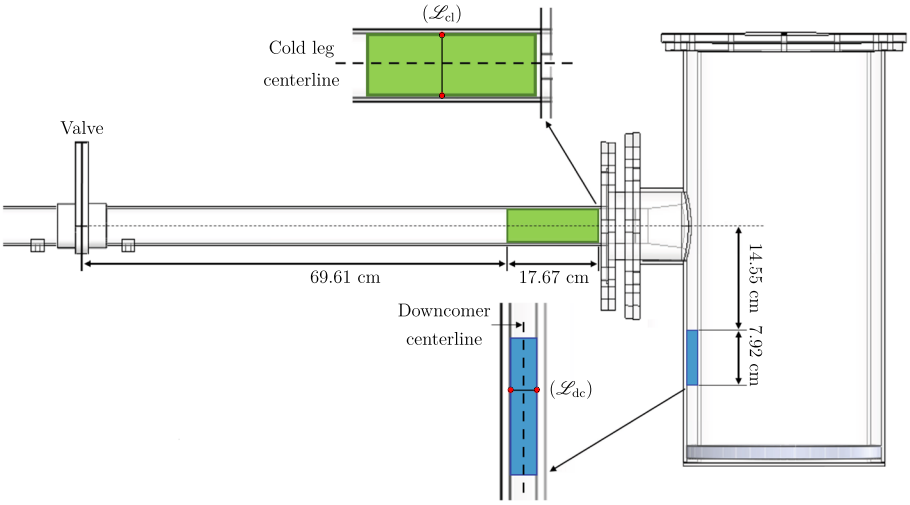

Fig. 2 Green: PIV measurement plane in the cold leg. Blue: PIV measurement plane in the downcomer. The lines $(\mathscr{L}_{cl})$ and $(\mathscr{L}_{dc})$, located respectively at $x = 77.45$ cm and $y = -17.56$ cm in the absolute frame of reference defined in Fig. 1, are used for plotting profiles in the cold leg and in the downcomer. Figure adapted from the benchmark specifications edited by the Texas A&M University

variable-density model described in the next section. The average values are found to remain approximately uniform in the cold leg (AB segment), and then show a variation induced simultaneously by a fluid acceleration caused by gravity and by the boundary layer height transition in the smooth nozzle (segment BC). Finally the values decrease slightly along the wall of the downcomer (segment CD), due the diffusion of the fluid in the annular volume. Higher RMS values of y^+ are observed in the downcomer compared to the cold leg, owing to a strongest turbulence. With the finest meshes $\mathscr{M}_3$ and $\mathscr{M}_4$, the average y^+ values remain lower than unity along the wall, which is the maximal value usually recommended for a wall-resolved LES. Further discussion about the mesh sensitivity and suitability is conducted in Sect. 4.1.

3 Turbulence Modeling and Numerical Framework

3.1 Governing Equations

The two fluids in presence are supposed to be miscible, so that the flow can be treated from a single-phase point of view without interface tracking. The single working fluid has

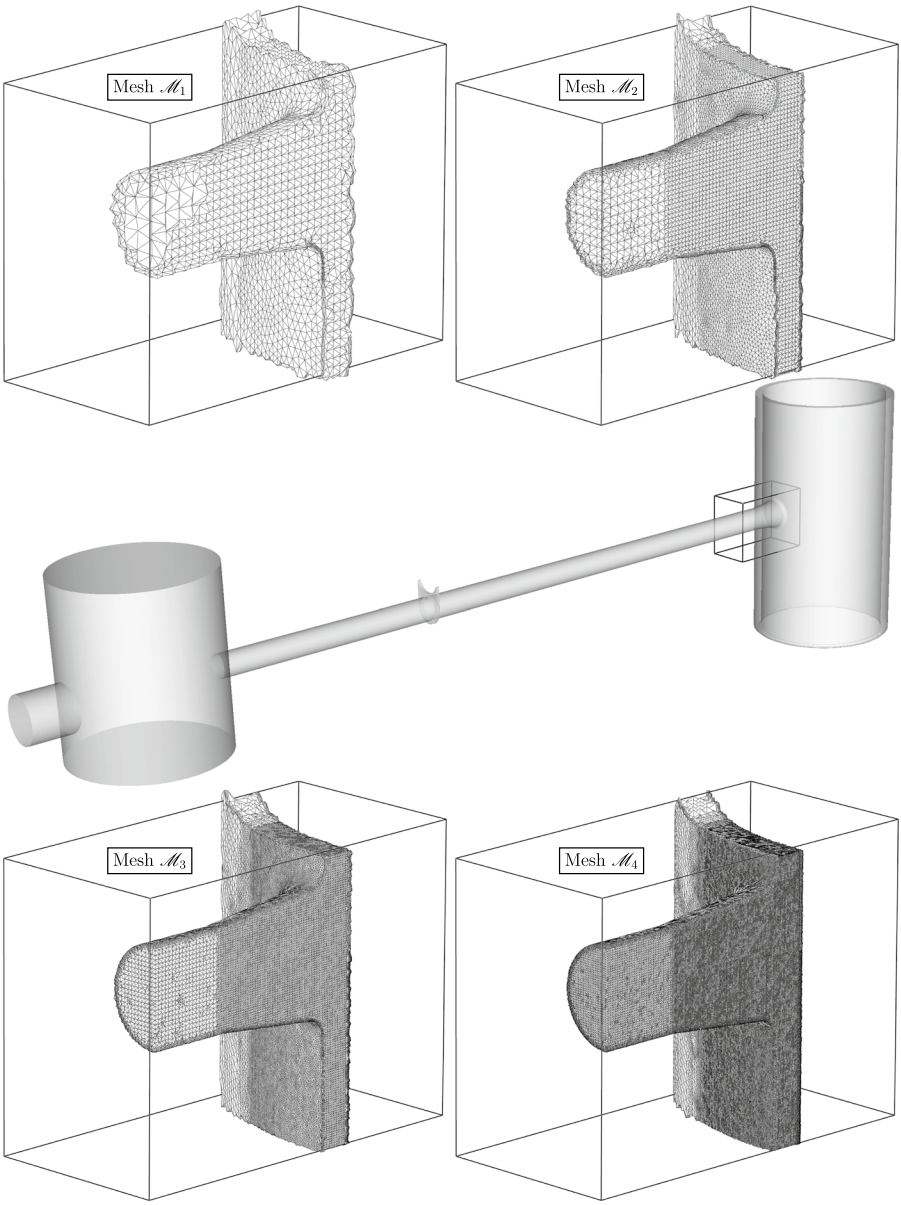

Fig. 3 Overview of the four tetraedral computational meshes used in the study: the meshes are shown in a box centered on the connection between the cold leg and the downcomer, and cutting the domain at $z = 0$

a variable density ρ and a dynamic viscosity μ both depending linearly on the heavy liquid mass fraction ϕ, which ranges between 0 (light liquid only) and 1 (heavy liquid only):

$$\mu = \phi\mu_H + (1 - \phi)\mu_L\,, \tag{3}$$

Table 2 Main characteristics of the four computational meshes

Mesh	$\mathscr{M}_1$	$\mathscr{M}_2$	$\mathscr{M}_3$	$\mathscr{M}_4$
Number of tetraedra	$5.77 \times 10^{+05}$	$3.00 \times 10^{+06}$	$1.79 \times 10^{+07}$	$1.16 \times 10^{+08}$
D.o.f. of concentration or velocity components	$1.18 \times 10^{+06}$	$6.09 \times 10^{+06}$	$3.61 \times 10^{+07}$	$2.33 \times 10^{+08}$
D.o.f. of pressure	$6.88 \times 10^{+05}$	$3.55 \times 10^{+06}$	$2.05 \times 10^{+07}$	$1.36 \times 10^{+08}$
Average tetraedra size in cold leg (m)	3.39×10^{-03}	1.83×10^{-03}	9.50×10^{-04}	4.80×10^{-04}
Average tetraedra size in downcomer (m)	1.79×10^{-03}	9.31×10^{-04}	4.81×10^{-04}	2.48×10^{-04}
Height of first prism layer in cold leg (m)	1.80×10^{-03}	9.00×10^{-04}	4.50×10^{-04}	2.25×10^{-04}
Height of first prism layer in downcomer (m)	8.00×10^{-04}	3.00×10^{-04}	1.50×10^{-04}	7.50×10^{-05}
Height of first prism layer in smooth nozzle (m)	4.00×10^{-04}	2.00×10^{-04}	1.00×10^{-04}	5.00×10^{-05}
Downcomer mesh size in the x- and z-directions ($\Delta x^+ = \Delta z^+$)	9.38	9.03	5.39	2.10
Downcomer mesh size in the y-direction ($\Delta y^+_{\min}$ – $\Delta y^+_{\max}$)	1.34–9.38	1.29–9.03	0.77–5.39	0.30–2.10

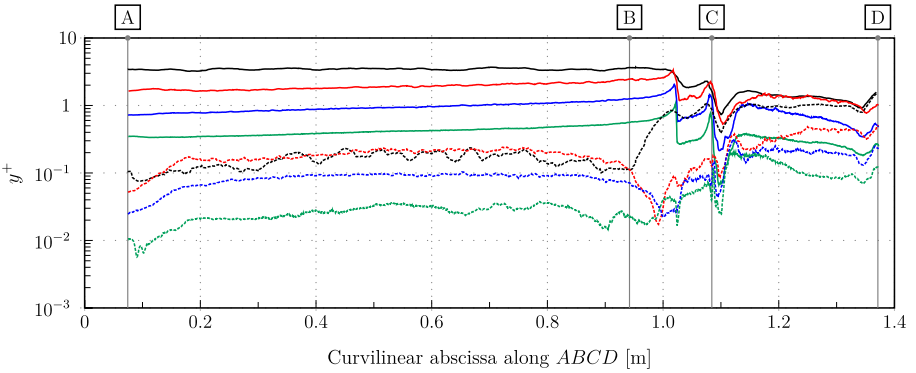

Fig. 4 Statistical values of y^+ in the time interval [10.84 s ; 20.84 s] along the ABCD wall line shown on Fig. 1c. The color code is as follows: —$\mathscr{M}_1$, —$\mathscr{M}_2$, —$\mathscr{M}_3$, —$\mathscr{M}_4$. Solid lines refers to the average values and dashed lines to the RMS values

$$\rho = \phi\rho_H + (1-\phi)\rho_L\,. \tag{4}$$

The latter assumptions of linear viscosity and density changes are experimentally well recovered (Orea et al. 2020). The governing equations in the gravity field for a newtonian fluid satisfying the Stokes' hypothesis write, under conservative formulation[1] (Chassaing et al. 2002):

(1) mass conservation equation:

[1] These equations are written here following the notational convention where the indices i and j are implicitly summed over when repeated.

$$\frac{\partial \rho}{\partial t} + \frac{\partial \rho u_i}{\partial x_i} = 0\,, \tag{5}$$

(2) momentum equation:

$$\frac{\partial \rho u_i}{\partial t} + \frac{\partial \rho u_i u_j}{\partial x_j} = -\frac{\partial p}{\partial x_i} + \frac{\partial \sigma_{ij}}{\partial x_j} + \rho g_i\,, \tag{6}$$

where the rate-of-strain tensor reads (Garnier et al. 2009)

$$\sigma_{ij} = \mu\left(\frac{\partial u_i}{\partial x_j} + \frac{\partial u_j}{\partial x_i} - \frac{2}{3}\frac{\partial u_k}{\partial x_k}\delta_{ij}\right), \tag{7}$$

(3) convection-diffusion of mass fraction:

$$\frac{\partial \rho \phi}{\partial t} + \frac{\partial \rho u_i \phi}{\partial x_i} = \frac{\partial q_i}{\partial x_i}\,, \tag{8}$$

with the following expression for the mass flux:

$$q_i = \frac{\mu}{\mathrm{Sc}}\frac{\partial \phi}{\partial x_i}\,. \tag{9}$$

The Schmidt number Sc quantifies the ratio between momentum diffusivity and mass diffusivity. Its value is not well defined for the working fluid and should even locally depend on the flow physics through a ϕ-dependence, but such a law of variation is unfortunately not known. In contrast to gases for which $\mathrm{Sc} \sim 1$, the tight arrangement of molecules in a liquid favors momentum transfers to the detriment of mass transfers, implying that $\mathrm{Sc} > 1$. Notwithstanding, it is uniformly set to unity in the present simulations. This input parameter was shown to have only a weak influence on the time-integrated quantities anyhow (Lai et al. 2020).

3.2 LES Modeling

Variable-density model (VD). As pointed out in Lai et al. (2019), the small value of the Batchelor length scale makes a true DNS presumably unreachable. Consequently the numerical resolution of the governing equations requires the introduction of a turbulence model. Given the highly unsteady and turbulent nature of the flow, LES is an appropriate option consisting in solving the large-scale motions while modeling the smallest scales. For this purpose, the large and small scales of the flow are separated by means of a spatial filtering operator. Nevertheless, for the LES of a compressible flow, the Favre filter is aptly used together with the spatial filter in order to substantially simplify the writing of the resulting filtered equations. The Favre operator is a density-weighted filter defined for any quantity F by: $\widetilde{F} = \overline{\rho F}/\bar{\rho}$. Applying the bar filter to the above governing equations, one readily obtains (Blazek 2015):

$$\frac{\partial \bar{\rho}}{\partial t} + \frac{\partial \bar{\rho}\widetilde{u}_i}{\partial x_i} = 0\,, \tag{10}$$

$$\frac{\partial \bar{\rho}\widetilde{u_i}}{\partial t} + \frac{\partial \bar{\rho}\widetilde{u_i}\widetilde{u_j}}{\partial x_j} = -\frac{\partial \bar{p}}{\partial x_i} + \frac{\partial \hat{\sigma}_{ij}}{\partial x_j} + \frac{\partial \mathcal{T}_{ij}^{\text{sgs}}}{\partial x_j} + \frac{\partial}{\partial x_j}\left(\bar{\sigma}_{ij} - \hat{\sigma}_{ij}\right) + \bar{\rho} g_i \,, \tag{11}$$

$$\frac{\partial \bar{\rho}\widetilde{\phi}}{\partial t} + \frac{\partial \bar{\rho}\widetilde{u_i}\widetilde{\phi}}{\partial x_i} = \frac{\partial \hat{q}_i}{\partial x_i} + \frac{\partial \mathcal{Q}_i^{\text{sgs}}}{\partial x_i} + \frac{\partial}{\partial x_i}\left(\bar{q}_i - \hat{q}_i\right), \tag{12}$$

where the computable rate-of-strain tensor and mass flux are:

$$\hat{\sigma}_{ij} = \mu\left(\frac{\partial \widetilde{u_i}}{\partial x_j} + \frac{\partial \widetilde{u_j}}{\partial x_i} - \frac{2}{3}\frac{\partial \widetilde{u_k}}{\partial x_k}\delta_{ij}\right), \tag{13}$$

$$\hat{q}_i = \frac{\mu}{\text{Sc}}\frac{\partial \widetilde{\phi}}{\partial x_i} \,. \tag{14}$$

The differences $\bar{\sigma}_{ij} - \hat{\sigma}_{ij}$ and $\bar{q}_i - \hat{q}_i$ are usually neglected (Meyers et al. 2008; Vreman et al. 1995, 1997). From the filtering operation arise the subgrid-scale stress tensor $\mathcal{T}_{ij}^{\text{sgs}} = \bar{\rho}(\widetilde{u_i u_j} - \widetilde{u_i}\widetilde{u_j})$ and mass flux vector $\mathcal{Q}_i^{\text{sgs}} = \bar{\rho}(\widetilde{u_i\phi} - \widetilde{u_i}\widetilde{\phi})$ in the momentum and mass fraction equations, respectively. Similarly to the molecular stress tensor (7), the Boussinesq scheme postulates a linear dependency of the deviatoric part of the subgrid-scale tensor with the resolved rate-of-strain tensor, namely

$$\mathcal{T}_{ij}^{\text{sgs}} - \frac{1}{3}\mathcal{T}_{kk}^{\text{sgs}} = \mu_{\text{sgs}}\left(\frac{\partial \widetilde{u_i}}{\partial x_j} + \frac{\partial \widetilde{u_j}}{\partial x_i} - \frac{2}{3}\frac{\partial \widetilde{u_k}}{\partial x_k}\delta_{ij}\right), \tag{15}$$

whereas the simple gradient diffusion hypothesis is used to close the mass fraction equation:

$$\mathcal{Q}_i^{\text{sgs}} = \frac{\mu_{\text{sgs}}}{\text{Sc}_t}\frac{\partial \widetilde{\phi}}{\partial x_i} \,. \tag{16}$$

These closure relationships introduce a subgrid-scale viscosity μ_{sgs}, which is afterwards evaluated by means of the WALE model (Nicoud and Ducros 1999). The turbulent Schmidt number Sc_t is usually close to unity, and is set here to 0.9. The isotropic part of the SGS stress tensor is included in a modified pressure $\bar{p}^*$. Finally, the variable-density or low-Mach number model is defined by the following set of three equations[2], supplemented by the empirical equations (3)–(4):

$$\frac{\partial \rho}{\partial t} + \frac{\partial \rho u_i}{\partial x_i} = 0 \,, \tag{17}$$

$$\frac{\partial \rho u_i}{\partial t} + \frac{\partial \rho u_i u_j}{\partial x_j} = -\frac{\partial p^*}{\partial x_i} + \frac{\partial}{\partial x_j}\left[(\mu + \mu_{\text{sgs}})\left(\frac{\partial u_i}{\partial x_j} + \frac{\partial u_j}{\partial x_i}\right)\right] + \rho g_i \,, \tag{18}$$

[2] To lighten the notations, the symbols for Favre average and filtered quantities are omitted from this point on.

$$\frac{\partial \rho\phi}{\partial t} + \frac{\partial \rho u_i \phi}{\partial x_i} = \frac{\partial}{\partial x_i}\left[\left(\frac{\mu}{\mathrm{Sc}} + \frac{\mu_{\mathrm{sgs}}}{\mathrm{Sc}_t}\right)\frac{\partial \phi}{\partial x_i}\right]. \tag{19}$$

Boussinesq approximation (BA) Although the VD model should be a fairly accurate representation of the real flow since the density variations are accounted for, it may be simplified for a buoyancy-driven flow with weak density changes (i.e. at small Atwood number). Let's set $\rho_0 = \rho(\phi_0)$, then the linearization of $\rho(\phi)$ at the point ϕ_0 yields

$$\rho(\phi) \approx \rho_0 + \frac{\partial \rho}{\partial \phi}(\phi_0)(\phi - \phi_0) = \rho_0\left[1 + \alpha_0(\phi - \phi_0)\right], \tag{20}$$

where $\alpha_0 = (\rho_H - \rho_L)/\rho_0$ is the coefficient of mass. A natural choice is to take $\phi_0 = 0.5$ and $\rho_0 = (\rho_H + \rho_L)/2$, implying that $\alpha_0 = 2\mathrm{A}$. The density in the convective terms is set to ρ_0 and the gravity potential in the momentum equation is included in the pressure term. Thus, the incompressible model derived from the Boussinesq approximation is defined by the set of equations below, now completed by Eq. (3) only:

$$\frac{\partial u_i}{\partial x_i} = 0, \tag{21}$$

$$\rho_0\left(\frac{\partial u_i}{\partial t} + \frac{\partial u_i u_j}{\partial x_j}\right) = -\frac{\partial p^*}{\partial x_i} + \frac{\partial}{\partial x_j}\left[(\mu + \mu_{\mathrm{sgs}})\left(\frac{\partial u_i}{\partial x_j} + \frac{\partial u_j}{\partial x_i}\right)\right] + \rho_0\alpha_0(\phi - \phi_0)g_i, \tag{22}$$

$$\rho_0\left(\frac{\partial \phi}{\partial t} + \frac{\partial u_i \phi}{\partial x_i}\right) = \frac{\partial}{\partial x_i}\left[\left(\frac{\mu}{\mathrm{Sc}} + \frac{\mu_{\mathrm{sgs}}}{\mathrm{Sc}_t}\right)\frac{\partial \phi}{\partial x_i}\right]. \tag{23}$$

In that case, the spatial and Favre filters are identical. Note also that in our simulations, the contribution $\mu \partial u_j/\partial x_i$ in the diffusion term of Eqs. (18) and (22) is neglected. In the following, the simulations using the Boussinesq Approximation or the Variable-Density model on mesh $\mathscr{M}_m$ will be referred to as BA_m or VD_m.

Boundary and initial conditions The system boundaries are seen as fixed walls without mass flux through them, which mathematically translates for the velocity and mass fraction unknowns into homogeneous Dirichlet ($\boldsymbol{u} = 0$) and Neumann ($\partial\phi/\partial n = 0$) boundary conditions, respectively. In order to numerically ensure the mass conservation in the whole system, a small opening with a prescribed uniform pressure ($p^* = 0$) is created at the top of the left-hand tank. With regards to the initial conditions, it was experimentally measured that the complete opening of the valve takes between 25 and 30 ms, albeit it is treated as instantaneous in the calculations. In addition, the small vortices created by the opening are ignored. The rationale for this simplification is twofold: firstly it would be difficult to introduce realistic effects of the very fast opening in the simulations, and secondly it was previously pointed out that it has no significant impact on the turbulence statistics in the cold leg and in the downcomer (Lai et al. 2019). As a consequence, the adopted initial conditions are mixtures at rest: $\boldsymbol{u} = 0$, and separated by the vertical plane $x = 0$: $\phi(x < 0) = 1$ and $\phi(x > 0) = 0$.

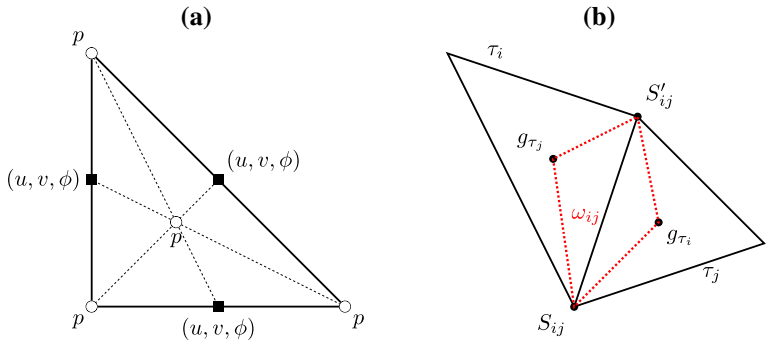

Fig. 5 2D representation of the FVE discretization. **a** Localisation of the degrees of freedom in the P_1NC-P_0P_1 element: the pressure points (p) are at the summits and center of the cell, and the velocity components (u, v) and scalar fields (here ϕ) at the center of the faces. **b** The control volume ω_{ij} is delimited by the summits S_{ij} and S'_{ij} shared by triangles τ_i and τ_j, and their barycenters g_{τ_i} and g_{τ_j}. The set of τ_i is the primal mesh and the set of ω_{ij} defines a dual staggered mesh

3.3 Numerical Framework

Finite Volume Element method. The simulations were conducted using the in-house CFD software TrioCFD[3] (Angeli et al. 2017; Calvin et al. 2002), in which a Finite Volume Element (FVE) discretization method is implemented. The FVE method is adapted for conformal triangular or tetraedral meshes and can be seen as a variant of the Crouzeix-Raviart non-conforming finite element method (Crouzeix and Raviart 1973), but with additional degrees of freedom for pressure. The resulting pressure discretization is P_0P_1 (Émonot 1992; Fortin 2006; Heib 2003) while the discretization of velocity and concentration remains P_1NC (unknowns located at the gravity center of the faces). To each face of the mesh is associated a control volume, as shown in Fig. 5. Similarly to the finite volume method, the local equations are then integrated on control volumes corresponding to the primal cells for mass conservation and to the dual cells for momentum conservation. Fluxes and differential operators are computed using finite element approximations, finally providing a matrix system to be solved. As shown in Heib (2003), the introduction of a piecewise affine pressure greatly improves the stability properties of the Crouzeix–Raviart element. The other interests of the method lie in its local conservation properties and the diagonal characteristic of the mass matrix.

Numerical schemes. An explicit Euler scheme was used for the temporal integration and a second order centered scheme for the diffusion operator. Regarding the convection terms, we have used a centered stabilized scheme adapted from Kuzmin and Turek (2004), where the discrete operator is splitted into a centered part and an upwind part, the weight of the latter being set to 0.2. Velocity and pressure are decoupled by means of a three-step prediction-correction method, where an intermediate velocity is first calculated and then corrected after computation of the pressure (Chorin 1968; Temam 1968). The algorithms used to solve the corresponding Poisson equation for pressure lean on the PETSc library: they either call on the direct Cholesky method based on a prior factorization of the pressure matrix, or on the preconditioned conjugate gradient method using a Symmetric Successive

[3] http://triocfd.cea.fr/

Over-Relaxation (SSOR) relaxation method. This choice depends mainly on the mesh size, the Cholesky method becoming too expensive and unusable beyond a certain number of degrees of freedom, which in pratice is the case from the mesh $\mathscr{M}_3$. At last, as the time step related to diffusion is much smaller than that related to convection (which results in a drop of the overall time step and unreasonably long simulations), the diffusion terms were implicited and the convection time step was used as the global time step. Despite the addition of inversion operations of a linear system, the global computational time was significantly decreased by this semi-implicit resolution procedure.

4 Results and Discussions

4.1 Mesh Sensitivity Analyses

With the aim of quantifying the mesh sensitivity of the numerical solutions, one introduces a normalized Root-Mean-Square Error (RMSE) for any quantity ψ computed by LES on two neighbouring meshes $\mathscr{M}_m$ and $\mathscr{M}_{m-1}$:

$$\mathscr{N}_k^{(m)}(\psi) = \frac{\mathscr{N}_k\left(\psi_{\text{LES}}^{(m)} - \psi_{\text{LES}}^{(m-1)}\right)}{\mathscr{N}_k\left(\psi_{\text{LES}}^{(m)}\right)}, \tag{24}$$

where the norm $\mathscr{N}_k$ is evaluated as

$$\mathscr{N}_k(\psi) = \frac{1}{N_k}\sqrt{\sum_{i\in\mathscr{P}_k}\psi_i^2}. \tag{25}$$

In the previous definitions, the index $k \in \{\text{cl;dc}\}$ refers to the location of the experimental measurement points, which are thus conveniently used to assess the mesh convergence. Furthermore, N_k is the number of experimental points in the set $\mathscr{P}_k$, averaged over the time interval $\mathscr{I}_k$. As a reminder, $N_{\text{cl}} = 1694$ and $N_{\text{dc}} = 1207$, which is supposed to be sufficiently large to provide representative RMSE.

Figure 6 shows the convergence of the viscosity ratio μ_{sgs}/μ in the cold leg and in the downcomer. The viscosity ratio is found out to converge towards zero w.r.t. the mesh size at least at order two, agreeing the observation made in Angeli (2019) for the WALE subgrid-scale model with the same CFD software. However, a noteworthy difference lies in the fact that the first mesh is in the asymptotic convergence zone for the cold leg case, contrary to the downcomer. In addition, the amplitude of the viscosity ratio reaches higher values in the downcomer. This difference may be attributed to a stronger turbulence in the downcomer than in the cold leg, requiring finer mesh cells.

Tables 3 and 4 gather the computed RMSE for mass fraction and velocity statistics. A monotonic convergence is noticed is most cases, except for U_{mean} in the downcomer, and for V_{sd} which shows a monotonic behavior only for the VD model in the downcomer. These quantities have a low order of magnitude, likely close to the one of the numerical errors, and would consequently require finer meshes and/or more accurate numerical schemes to reach a monotonic convergence area. Besides it can't be inferred from these values that mesh convergence is reached, the relative discrepancy between $\mathscr{M}_3$ and $\mathscr{M}_4$ being seldom lower than 10%, especially in the downcomer.

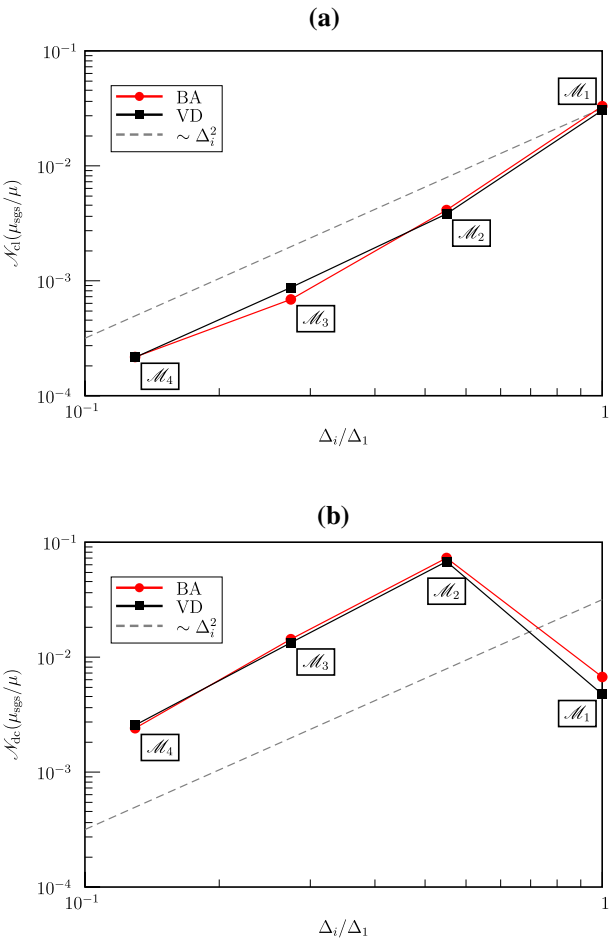

Fig. 6 Mesh convergence of the viscosity ratio for BA and VD models in **a** the cold leg and **b** the downcomer, where Δ_i for $i \in \{1;2;3;4\}$ is the average mesh size in the area under consideration. The observed convergence order w.r.t. the mesh size is about two

Table 3 RMSE between two consecutive meshes for various quantities of interest in cold leg and downcomer, in the case of the BA model

ψ	$\phi_{\rm mean}$	$\phi_{\rm sd}$	$U_{\rm mean}$	$U_{\rm sd}$	$V_{\rm mean}$	$V_{\rm sd}$
$\mathscr{N}_{\rm cl}^{(2)}(\psi)$	8.99×10^{-01}	2.70×10^{-01}	6.33×10^{-01}	2.93×10^{-01}	9.99×10^{-01}	2.62×10^{-01}
$\mathscr{N}_{\rm cl}^{(3)}(\psi)$	1.27×10^{-01}	2.20×10^{-01}	9.98×10^{-02}	1.52×10^{-01}	9.10×10^{-01}	2.01×10^{-01}
$\mathscr{N}_{\rm cl}^{(4)}(\psi)$	4.17×10^{-02}	9.77×10^{-02}	7.23×10^{-02}	9.18×10^{-02}	7.70×10^{-01}	2.19×10^{-01}
$\mathscr{N}_{\rm dc}^{(2)}(\psi)$	$1.82\times10^{+00}$	3.91×10^{-01}	$1.47\times10^{+00}$	$7.67\times10^{+00}$	$1.21\times10^{+00}$	1.22×10^{-01}
$\mathscr{N}_{\rm dc}^{(3)}(\psi)$	2.22×10^{-01}	1.19×10^{-01}	6.84×10^{-01}	2.67×10^{-01}	1.80×10^{-01}	1.73×10^{-01}
$\mathscr{N}_{\rm dc}^{(4)}(\psi)$	1.19×10^{-01}	9.13×10^{-02}	8.57×10^{-01}	1.65×10^{-01}	9.98×10^{-02}	1.87×10^{-01}

Table 5 gathers information on the actual computational costs of the simulations. The reported time step is the average for $0 < t < 20.84$ s of the overall stability time step computed by the code. A local stability time step is calculated as the harmonic mean of a

Table 4 RMSE between two consecutive meshes for various quantities of interest in cold leg and downcomer, in the case of the VD model

ψ	ϕ_{mean}	ϕ_{sd}	U_{mean}	U_{sd}	V_{mean}	V_{sd}
$\mathcal{N}_{\text{cl}}^{(2)}(\psi)$	7.99×10^{-01}	2.75×10^{-01}	5.82×10^{-01}	3.10×10^{-01}	9.81×10^{-01}	2.82×10^{-01}
$\mathcal{N}_{\text{cl}}^{(3)}(\psi)$	1.02×10^{-01}	2.65×10^{-01}	8.98×10^{-02}	1.79×10^{-01}	8.70×10^{-01}	2.16×10^{-01}
$\mathcal{N}_{\text{cl}}^{(4)}(\psi)$	6.35×10^{-02}	1.03×10^{-01}	4.96×10^{-02}	8.10×10^{-02}	5.69×10^{-01}	2.70×10^{-01}
$\mathcal{N}_{\text{dc}}^{(2)}(\psi)$	$1.36\times10^{+00}$	2.28×10^{-01}	$1.05\times10^{+00}$	$7.60\times10^{+00}$	9.23×10^{-01}	2.03×10^{-01}
$\mathcal{N}_{\text{dc}}^{(3)}(\psi)$	2.26×10^{-01}	1.22×10^{-01}	6.91×10^{-01}	2.57×10^{-01}	2.00×10^{-01}	1.80×10^{-01}
$\mathcal{N}_{\text{dc}}^{(4)}(\psi)$	1.21×10^{-01}	4.97×10^{-02}	7.49×10^{-01}	1.23×10^{-01}	1.18×10^{-01}	1.65×10^{-01}

Table 5 Computational costs raised in each case, from 0 to 20.84 physical seconds

Mesh	$\mathcal{M}_1$	$\mathcal{M}_2$	$\mathcal{M}_3$	$\mathcal{M}_4$
Average time step (BA) (s)	1.43×10^{-03}	5.17×10^{-04}	2.48×10^{-04}	1.15×10^{-04}
Average time step (VD) (s)	1.34×10^{-03}	5.01×10^{-04}	2.49×10^{-04}	1.12×10^{-04}
Normalized CPU cost (BA)	$1.00\times10^{+00}$	$2.69\times10^{+01}$	$3.69\times10^{+02}$	$5.32\times10^{+03}$
Normalized CPU cost (VD)	$1.33\times10^{+00}$	$3.90\times10^{+01}$	$8.03\times10^{+02}$	$2.05\times10^{+04}$
Calculation time (BA) (h)	5.95	30.44	69.95	155.59
Calculation time (VD) (h)	7.87	44.08	152.15	598.54
Number of CPUs used	19	100	596	3866

convective and a diffusive time step, and the overall stability time step used is the minimum of the local time steps. This adaptive time-stepping procedure ensures that the CFL and Fourier stability conditions are satisfied in the whole domain at every moment of the simulation. The calculations were performed on the Skylake Irene partition of the Joliot-Curie supercomputer. Details on the computer architecture can be found at http://www-hpc.cea.fr/en/complexe/tgcc-JoliotCurie.htm. Table 5 indicates in particular that the simulation VD_4 required about 15,000 times more CPU hours than VD_1, and lasted 76 times longer. Consequently, even if there is room for improvement of the results and mesh convergence in the downcomer, a simulation on a fifth mesh would be unreasonably long and grossly expensive, and was not attempted.

4.2 Global Flow Analysis

The flow has two distinct stages: at the moment where the valve is opened, a buoyancy-driven flow develops in the cold leg with a front advancing towards the downcomer. After a while, the heavy fluid begins to discharge into the downcomer, generating a strong turbulent mixing. The flow development up to 20.84 physical seconds is illustrated by a video of the simulation VD_4, available at https://triocfd.cea.fr/databases/CLM_database.

Fluid front displacement in the cold leg Figure 7 shows the fluid front advance in the downcomer during the first 10 s. It can be observed that the convective velocity reaches quickly a constant value, around 0.1 m/s. The propagation velocity is controlled by the Atwood number: the temporal evolution of the concentration field on Fig. 8b indicates

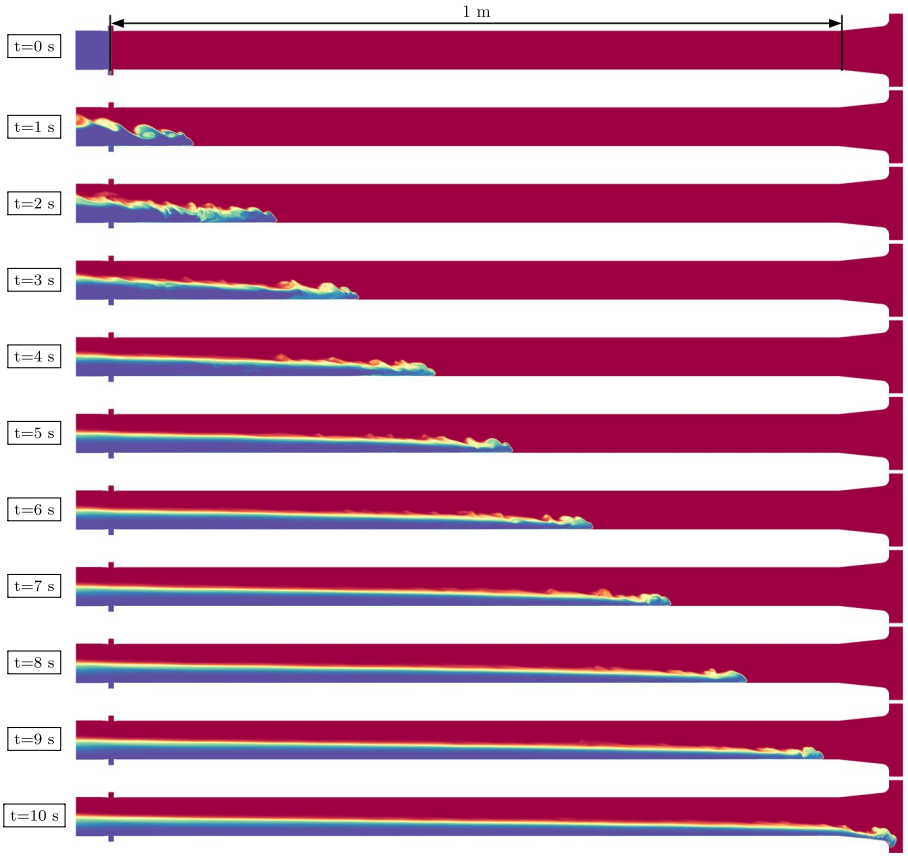

Fig. 7 Sequence of snapshots showing the evolution of the heavy fluid mass fraction in the cold leg obtained by the VD_4 simulation. The colour scale goes from 0 (red) to 1 (blue)

that the front moves about 36% faster with an Atwood number of $A = 0.1$ compared to $A = 0.05$. This is due to largest buoyancy forces if the density difference increases, even if the shape of the time evolution is very similar in both cases. Figure 8b gives the time when the gravity current reaches the point CL_1, located at 73.68 cm from the valve, for two values of the Atwood number. It can be deduced that the propagation velocity u_H is proportional to $\sqrt{gRA}$, where $R = 2.66$ cm is the radius of the horizontal tube and the constant of proportionality is about 1.30. This law is in fair agreement with the theoretical solution of Benjamin whose constant is $\sqrt{2} \approx 1.41$ (Benjamin 1968).

In addition to the Atwood number, the densimetric Froude and Richardson numbers Fr and Ri step also in the flow. They are estimated from

$$\mathrm{Fr} = \frac{1}{\sqrt{\mathrm{Ri}}} = \sqrt{\frac{\rho_0}{\rho_H - \rho_L}} \frac{U_0}{\sqrt{gL_0}} \tag{26}$$

Taking A = 0.05, $U_0 = 0.1$ m/s and chosing the characteristic length scale L_0 as the cold leg diameter ($L_0 = 2R = 0.0532$ m), one obtains Fr = 0.43 and Ri = 5.40. These values indicate that the flow in the cold leg is mainly driven by buoyancy forces, although inertia

effects can't be completely neglected. It should be noted that the density ratio of the fluids was adjusted in the scale-down experimental test facility to obtain Fr and Ri matching real reactor conditions. Figure 8a and c show that during the transient stage in the cold leg, a counterflow with waves propagating both to the right and to the left appears, as well as a Kelvin–Helmholtz instability giving rise to spiral structures. As these whorls are small-sized and rapidly evolving, a fine mesh and a small time step are required to capture them, what meshes $\mathscr{M}_1$ and $\mathscr{M}_2$ fail to achieve. Note however that the meshes 2, 3 and 4 give very close crossing times for both BA and VD models, *i.e.* around 10 s to reach the downcomer.

The time evolution of the horizontal component of velocity in Fig. 8c–e reveals the chronology of the flow development: in the main flow, the wave arrival creates strong and fast velocity variations followed by very small turbulent fluctuations that end up gradually disappearing. On the contrary, the counterflow exhibits only low-frequency ripples and almost no turbulence. Thus the simulations show that the main flow goes through a short phase of weak turbulence which occurs at the shear layer between the heavy and light phases where ϕ is around 0.5, and the back flow remains laminar. It can also be noted that VD and BA models exhibit very similar trends, likely because the Atwood number is low.

Turbulent mixing in the downcomer The heavy liquid starts to fall down in the downcomer after about 10 s, with a separation point located near the point C of Fig. 1. The drop is accompanied by a diffusion in the annular space of the downcomer and the onset of turbulence. Between 12 and 13 s, the heavy liquid is mainly concentrated close to the vertical external wall, then ends up detaching and impacting the internal wall. This process is represented on Fig. 9.

Moreover, some whirls induced by the Kelvin-Helmholtz instability can be seen on Fig. 10, for example at $t = 20$ s, similarly to the cold leg. For the evaluation of the dimensionless numbers in the downcomer, the typical length scale L_0 may be chosen as the gap between internal and external walls, namely $L_0 = 0.019$ m. Besides, the characteristic velocity is $U_0 = 0.25$ m/s. The Richardson number is then Ri = 0.32 and the turbulent behavior is thus triggered by the mutual competition between inertia and buoyancy effects.

Figure 11 shows the temporal evolution of the vertical component of velocity in several points specified in Fig. 10, and clearly highlights the turbulent fluctuations in the downcomer. A stronger turbulence is observed near the inner wall compared to the outer wall, characterized by a richer frequency content. This is examined in more detail through the spectral analysis that follows.

4.3 Spectral Analysis in Downcomer

In order to perform a spectral analysis, the temporal data of velocity are collected at monitor points DC_1, DC_2 and DC_3 in the downcomer, whose location is given in Fig. 10. The computed signals are represented in Fig. 11. According to the Taylor' frozen turbulence hypothesis, the wavenumber power spectrum can be approximated from this data by converting the wavenumber into time frequency with the use of the average convective velocity. Note however that this time-space transformation is not rigorously valid in the present case, since the quadratic mean of velocity is not negligible in front of the average velocity. We compute here the frequency spectrum, which is the square of the Fourier transform of the velocity signal, or equivalently the Fourier transform of the autocorrelation function, because the latter is the convolution product of the temporal signal with itself. The Fast Fourier Transform (FFT) of the velocity signals of Fig. 11 is performed over the time interval [15 s; 20 s] where the turbulence can be considered as statistically stationary, and

Fig. 8 Series of plots for the case $A = 0.05$. **a** Mass fraction in cold leg at $t = 6$ s, for 0.4 m $< x <$ 0.9 m, **b** ▶ time evolution of the mass fraction at point CL_1 with comparison to the case $A = 0.10$, **c** time evolution of the horizontal velocity at points CL_1, CL_2 and CL_3, **d** zoom of the horizontal velocity at point CL_1, **e** zoom of the horizontal velocity at point CL_2

the Hann window function is applied on the corresponding finite length signal. The result shown on Fig. 12 provides some useful insight into the turbulent mechanisms at work and the quality of LES resolution. According to Fig. 12, the energy drops by several orders of magnitude, implying that the grid resolution of mesh $\mathscr{M}_4$ is high enough to capture a large range of turbulent eddies. The shape of the spectrum suggests a phenomenon of energy cascade, where the kinetic energy is transferred from large to small scales of the flow. Moreover, the slope in −5/3 in the intermediate frequencies indicates the existence of an inertial subrange in agreement with the Kolmogorov' hypotheses. For the mesh $\mathscr{M}_4$, the conversion of the spatial resolution of 2.5×10^{-4} m into time frequency using an average advection velocity of approximately 0.2 m/s yields a resolution up to 800 Hz. This value is consistent with the strong dissipation of energy observed at frequencies above 800 Hz, corresponding to the range taken into account by the SGS model.

In the next two sections, comparisons between experimental measurements and numerical simulations are carried out.

4.4 Validation in the Cold Leg

For the quantities of interest, Fig. 13 summarizes the experimental sets of measurements converted into 2D maps as well as the CFD results obtained with the different meshes in the cold leg. It appears immediately that meshes $\mathscr{M}_3$ and $\mathscr{M}_4$ achieve globally a good agreement with experiment. Moreover, both models lead to fairly similar solutions, but the largest discrepancy is obtained on the vertical components V_{mean} and V_{sd} which are of low magnitude compared to the streamwise components U_{mean} and U_{sd}.

The observation of some profiles plotted on Fig. 14 provides confirmation of this analysis. The streamwise components U_{mean} and U_{sd} match very well with PIV, although both models underestimate a little the fluctuations in the back flow. Interestingly, and as previously underlined, the vertical components are not as well predicted, particularly with regard to V_{mean} with the BA model which is unable to issue a correct intensity. On the other hand, the global shape of V_{mean} with the VD model, and of V_{sd} with both models, is correctly reproduced, but with a shifted peak of the fluctuations. It may be again argued that a finer mesh would be required to get closer to the measured values, because these two quantities have a low magnitude and show the largest RMSE between $\mathscr{M}_3$ and $\mathscr{M}_4$, as shown in Tables 3 and 4, suggesting that the mesh convergence is not fully reached. By the way, note that the maximum PIV measurement errors assessed in Orea et al. (2020) are 0.00276 m/s for U_{mean} and 0.0000261 m/s for V_{mean}. Hence, the calculated values of V_{mean} go distinctly beyond the uncertainty bars in places, contrary to U_{mean}. Regardless, the VD model seems on the whole to perform slightly better in the cold leg than the BA model.

4.5 Validation in the Downcomer

In the downcomer, the quantities of primary interest are V_{mean} as well as the standard deviations, because the velocity values in horizontal direction are very small compared

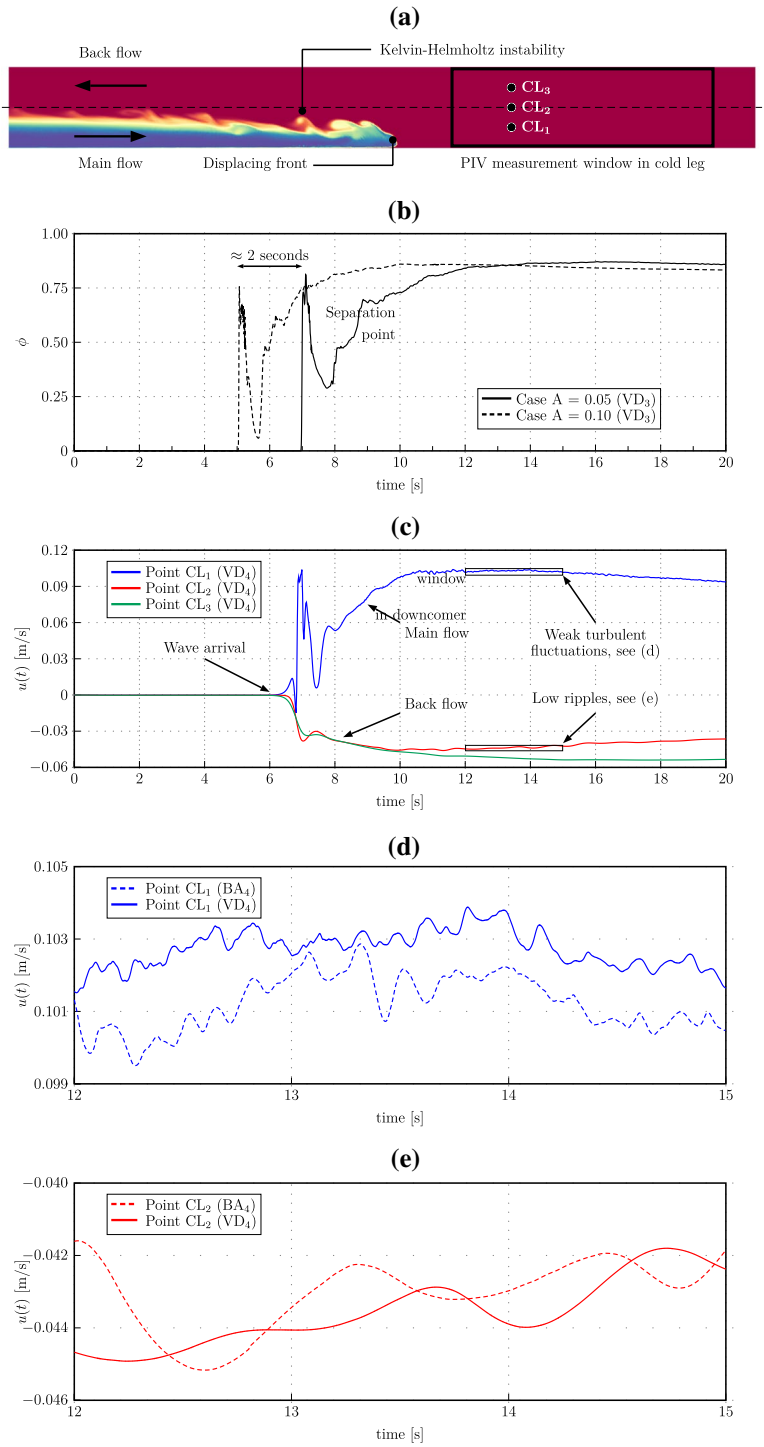
(a)
Back flow
Kelvin-Helmholtz instability
CL3
CL2
CL1
Main flow
Displacing front
PIV measurement window in cold leg
(b)
≈ 2 seconds
Separation point
Case A = 0.05 (VD3)
Case A = 0.10 (VD3)
time [s]
(c)
Point CL1 (VD4)
Point CL2 (VD4)
Point CL3 (VD4)
window
in downcomer
Main flow
Weak turbulent fluctuations, see (d)
Wave arrival
Back flow
Low ripples, see (e)
u(t) [m/s]
time [s]
(d)
Point CL1 (BA4)
Point CL1 (VD4)
u(t) [m/s]
time [s]
(e)
Point CL2 (BA4)
Point CL2 (VD4)
u(t) [m/s]
time [s]

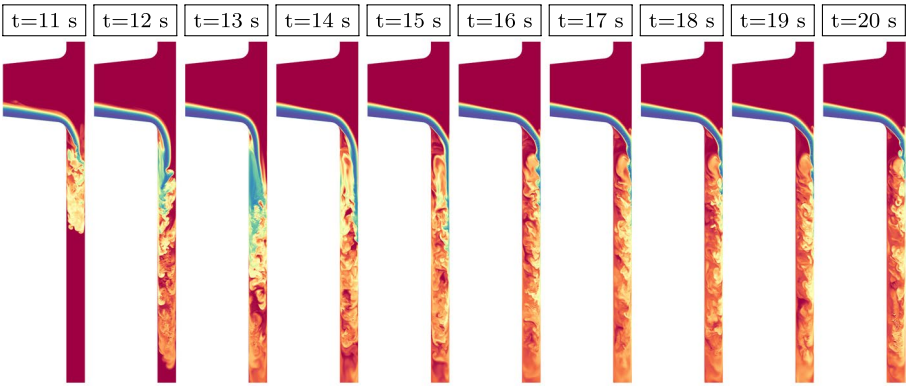

Fig. 9 Sequence of snapshots showing the evolution of the heavy fluid mass fraction in the downcomer obtained by the VD_4 simulation. The colour scale goes from 0 (red) to 1 (blue)

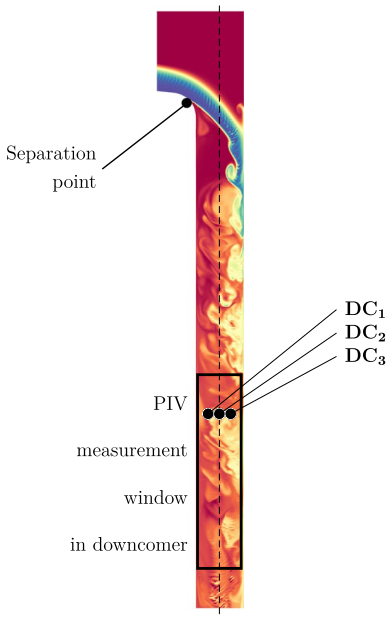

Fig. 10 Mass fraction of heavy liquid in downcomer at $t = 20$ s for $-0.24\ \text{m} < y < 0$, predicted by the VD_4 simulation

to the vertical direction. Figure 15 displays the computed fields on the four meshes under consideration in comparison with the PIV measurements. In spite of their relevance to assist the comprehension of the mixing process, azimuthal quantities were unfortunately not measured. In accordance with Sect. 4.1, it can be outlined from this figure that the solutions show a strong sensitivity to the mesh, particularly regarding the component U_{mean}. Except for this quantity, VD and BA models look relatively close to each other and a correct agreement with the measurements seems to be achieved overall, although this is not the case for the whole section. This is particularly true for U_{sd} and V_{mean}, where the PIV points exhibit respectively large values at the top and the bottom of the window, and low values close to the walls, which are not met in the VD_4 and BA_4

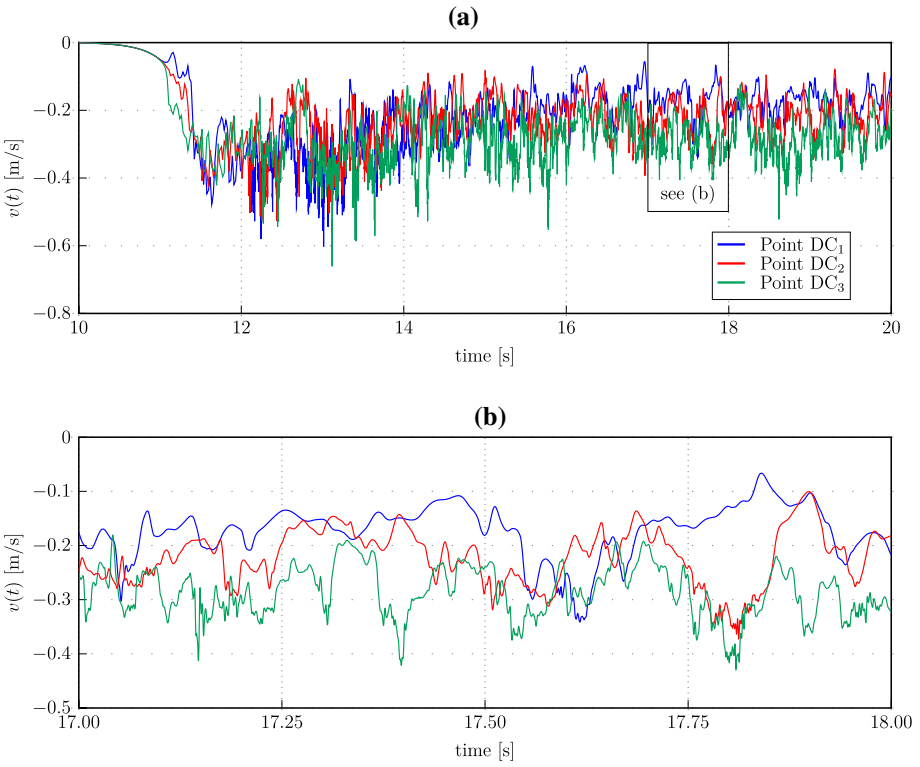

Fig. 11 **a** Temporal evolution of the instantaneous vertical velocity component in the downcomer obtained by simulation VD_4 in several points showed in Fig. 10, **b** zoom on a temporal window of 1 s

simulations. Incidentally, certain anomalies in the measurements can be observed; in particular, the existence of nearly zero values of the fall velocity at the bottom of the measurement window remains unexplained and in all likelihood unphysical. This leads us to be cautious in interpreting the differences between experiment and calculations.

The profiles along the horizontal line ($\mathscr{L}_{dc}$) are plotted on Fig. 16. They reveal that the average fall velocity V_{mean} agrees quite well with the experimental points, in spite of a wrong representation of near-wall gradients. The shape of the V_{mean} profiles is very similar to the results shown in Lai et al. (2019). It is further observed a poor prediction of U_{mean}, even more disappointing with VD model than with BA model, since the centerline values are strongly overestimated. In this respect, experimental measurements of the spanwise component W_{mean} in the downcomer would have been of great interest to help analyzing the heavy liquid diffusion in the downcomer, especially in order to check the mass fluxes distribution. A possible explanation for the apparently disappointing prediction of U_{mean} is that, as will be shown in paragraph Sect. 4.6, the location of the PIV window coincide with a sharp peak of the horizontal velocity. As a consequence, a small uncertainty on the peak location would strongly modify the amplitude of U_{mean}. It would also allow to understand why the VD and BA solutions, which are close together for all other quantities, show a larger discrepancy for the U_{mean} variable. Anyhow, the measurement uncertainty in the downcomer of 0.000022 m/s for U_{mean} and 0.0031 m/s for V_{mean} stated in Orea et al. (2020) can't supply any justification for

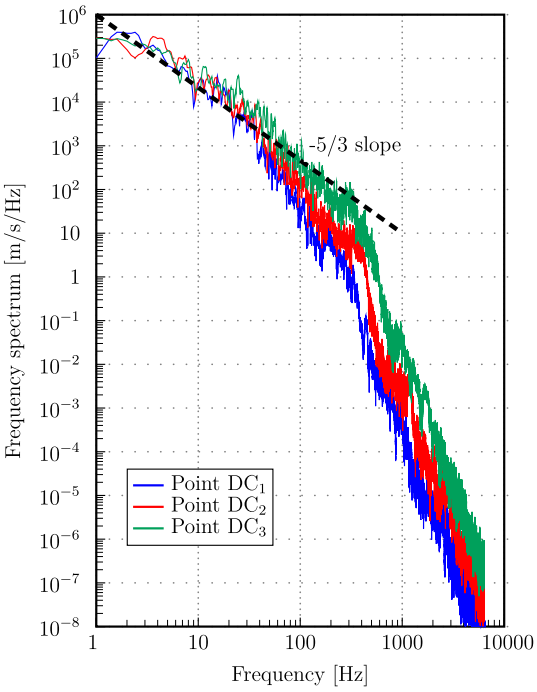

Fig. 12 Frequency spectra for the fluctuating component of the vertical velocity at several monitor points for 15 s < t < 20 s (VD_4 simulation)

the observed discrepancy, although these values seem optimistic in view of the experimental fields shown on Figs. 13 and 15 and suggesting systematic errors on the experimental data. Moreover, an excellent agreement is obtained for the standard deviations U_{sd} and V_{sd}, which is particularly true for the horizontal component. VD and BA models behave differently for V_{sd}: the first one is more consistent close to the outer wall, while the contrary occurs with the second one. Finally, the BA model yields slightly more accurate results in the downcomer, though they actually mainly distinguish by the quantity U_{mean}.

4.6 Velocity Distribution in the Downcomer

Regrettably, no experimental measurements of the velocity or the concentration distributions in the annular space of the downcomer are available. Nevertheless, the plot of radial and azimuthal quantities stemming from the numerical simulations helps providing additional insight on how the mixing occurs. Figure 17 gives the instantaneous mass fraction ϕ in two different views in the downcomer. It shows that the downcomer begins to fill with heavy liquid below the cold leg outlet, causing an up-flow on the opposite side, and that the strongest turbulent fluctuations take place just below the junction between the pipe and the downcomer.

A convenient frame to discuss the flow distribution in the downcomer is the cylindrical coordinate system ($\mathbf{e}_r$; $\mathbf{e}_\theta$; $\mathbf{e}_{z'}$) defined in Fig. 18 along a circular path ($\mathscr{C}$). In this system, the velocity vector averaged over the time interval $\mathscr{I}_{dc}$ writes: $\mathbf{U}_{mean} = U_{r,mean}\mathbf{e}_r + U_{\theta,mean}\mathbf{e}_\theta + U_{z',mean}\mathbf{e}_{z'}$ where

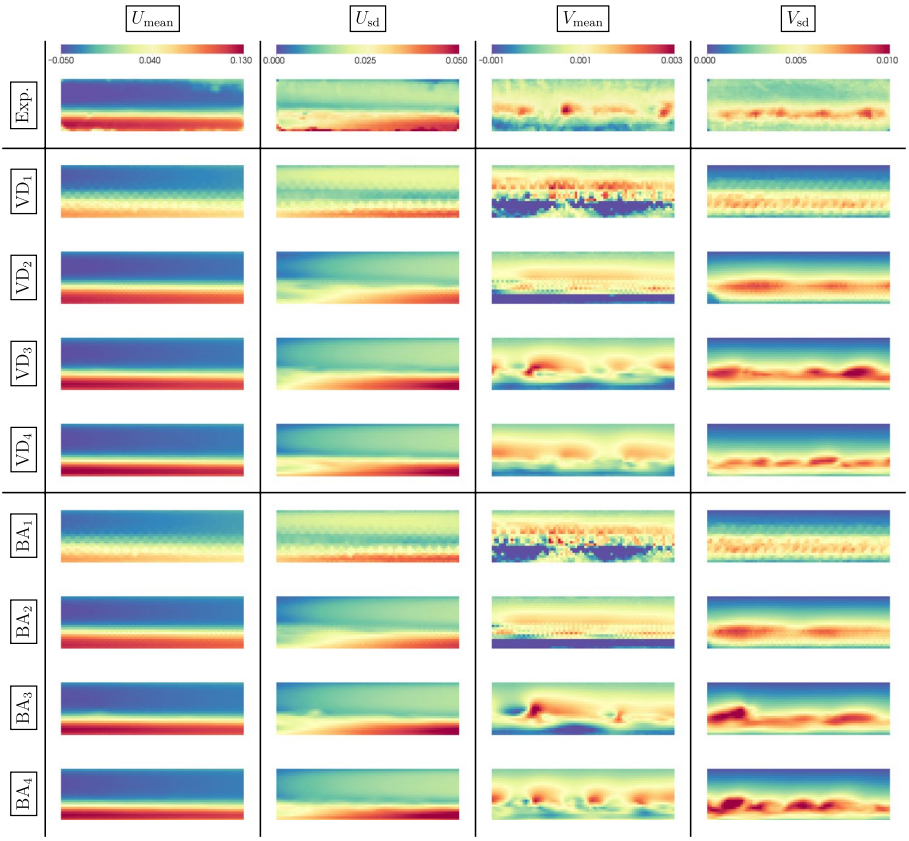

Fig. 13 Comparisons between the experimental measurements and the numerical solutions of the simulations in the cold leg (green window of Fig. 2). The CFD fields are interpolated on the experimental points coordinates. The legends are in m/s

$$\begin{cases} U_{r,\text{mean}} &= U_{\text{mean}} \cos\theta - W_{\text{mean}} \sin\theta\,, \\ U_{\theta,\text{mean}} &= -U_{\text{mean}} \sin\theta - W_{\text{mean}} \cos\theta\,, \\ U_{z',\text{mean}} &= V_{\text{mean}}\,. \end{cases} \tag{27}$$

Figure 19 shows that the radial velocity $U_{r,\text{mean}}$ exhibits a large positive peak at $\theta = 180°$, so that a slight deviation from this position would lead to a very different amplitude. The strong sensitivity around this azimuthal position, where $U_{r,\text{mean}} \approx -U_{\text{mean}}$, could explain the significant difference between simulations and experiments observed for U_{mean} in Fig. 16. The radial velocity increases up to a maximum value at $\theta \approx 140°$ and $\theta \approx 220°$, then logically changes sign at $\theta \approx 90°$ and $\theta \approx 270°$. The azimuthal and vertical velocity components are plotted on Fig. 20, from which it may be observed that $U_{\theta,\text{mean}}$ varies smoothly with the angle θ while the magnitude of $U_{z',\text{mean}}$ increases drastically below the cold leg opening. There is consequently a strong downward motion. The positive values of $U_{z',\text{mean}}$ outside the close vicinity of $\theta = 180°$ mean that an average reverse flow is formed between 10.84 s and 20.84 s, having a maximum

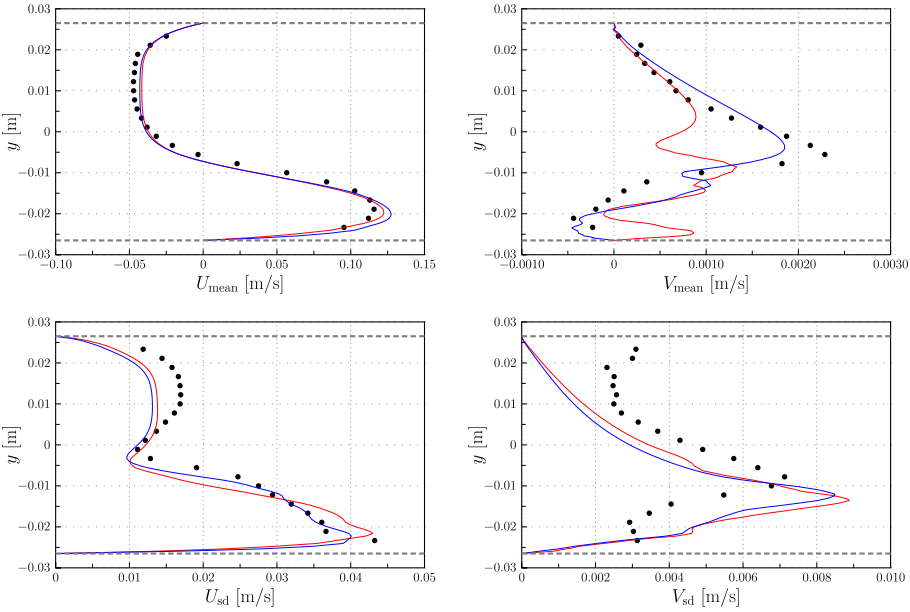

Fig. 14 Plots of the average horizontal and vertical components of the velocity, and their standard deviations, along the line ($\mathscr{L}_{\text{cl}}$) of Fig. 2. The legend is as follows: • Experiment, — Simulation BA_4, — Simulation VD_4. The dashed lines represent the walls of the pipe

intensity at $\theta \approx 0°$. Figure 21 confirms that, as mentioned above, the strength of turbulence characterized by the turbulent kinetic energy defined as

$$\mathcal{K} = \frac{1}{2}\left(U_{\text{sd}}^2 + V_{\text{sd}}^2 + W_{\text{sd}}^2\right), \tag{28}$$

is the strongest at $\theta = 180°$, but has also a local maximum near $\theta = 0$, which is the location where the flows coming from both sides of the downcomer meet and thus produce an increase in the turbulent mixing. Finally, it is worth noting from these plots that both physical models under consideration agree well with each other.

5 Summary and Conclusions

This work was part of a benchmark exercise carried out under the auspices of OECD/NEA. It was devoted to the numerical study of mixing of two miscible liquids in a test facility replicating a Pressurized Thermal Shock scenario in a pressurized water nuclear reactor. Wall-resolved LES of this transient density-driven flow were conducted, with the primary goals to analyze the flow mechanism, assess the numerical sensitivity to the mesh and to the physical model, perform validation against experimental measurements and finally assist the understanding of the fluid mixing mechanism in a PTS event.

The two-phase problem was numerically solved within a single-fluid framework using a mass fraction which interpolates the uniform density and viscosity of each

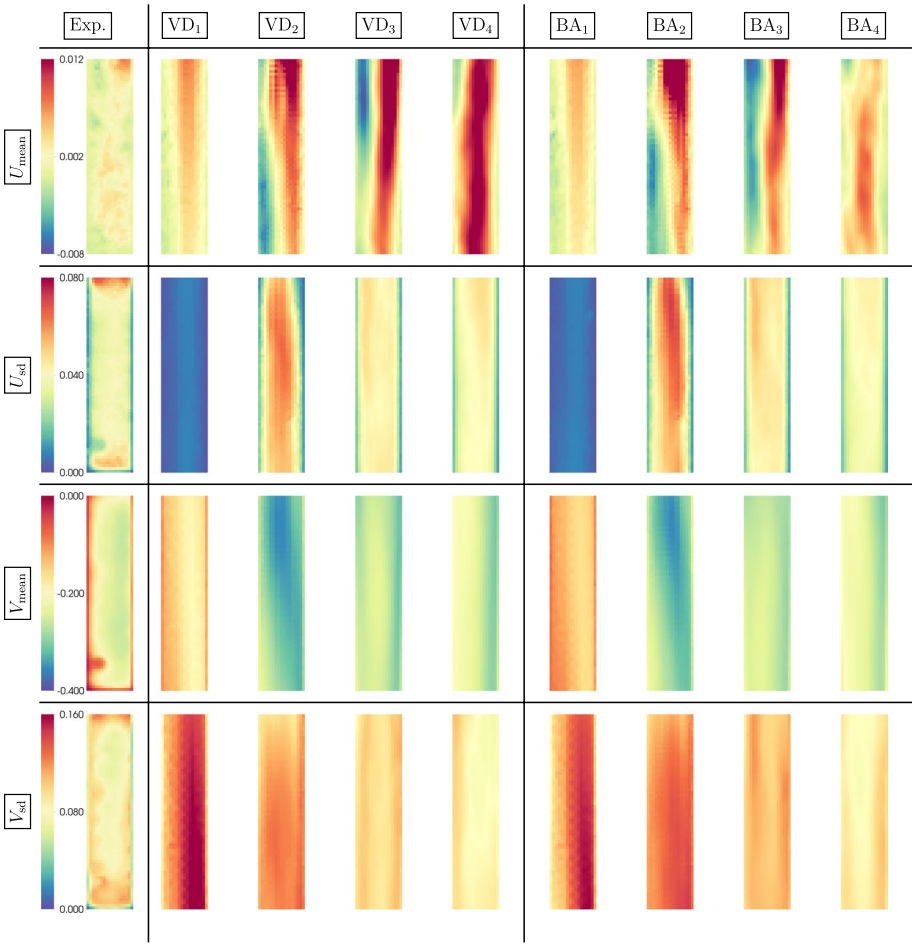

Fig. 15 Comparisons between the experimental measurements and the numerical solutions of the simulations in the downcomer (blue window of Fig. 2). The CFD fields are interpolated on the experimental points coordinates. The legends are in m/s

phase. Two physical models were compared, one using a density that is a function of the mass fraction of the heavy fluid, the other assuming a uniform density. The WALE subgrid-scale model was considered, and constant values for the molecular and turbulent Schmidt numbers were used in the physical modeling. Although these parameters are a source of uncertainty, their effect was not investigated in the present work. Experimental data are available up to 70 s, but due to the high computational cost, only the early phase of the experiment was studied and the simulations were carried out up to a physical time of 20.84 s. We have strived to evaluate the sensitivity of the solutions with respect to the meshing by using four grids progressively refined. The discrepancy between consecutive meshes was assessed using RMSE metrics, and the time-averaged velocities as well as second-order flow statistics were compared to experimental data.

The main conclusions that can be drawn from this study are the following:

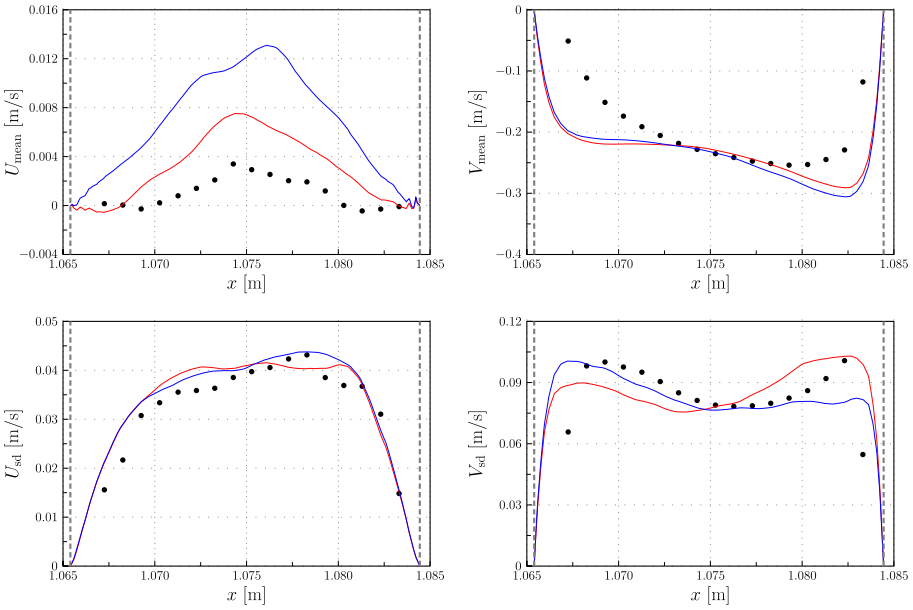

Fig. 16 Plots of the average horizontal and vertical components of the velocity, and their standard deviations, along the line ($\mathscr{L}_{\text{dc}}$) of Fig. 2. The legend is as follows: • Experiment, — Simulation BA_4, — Simulation VD_4. The dashed lines represent the downcomer walls

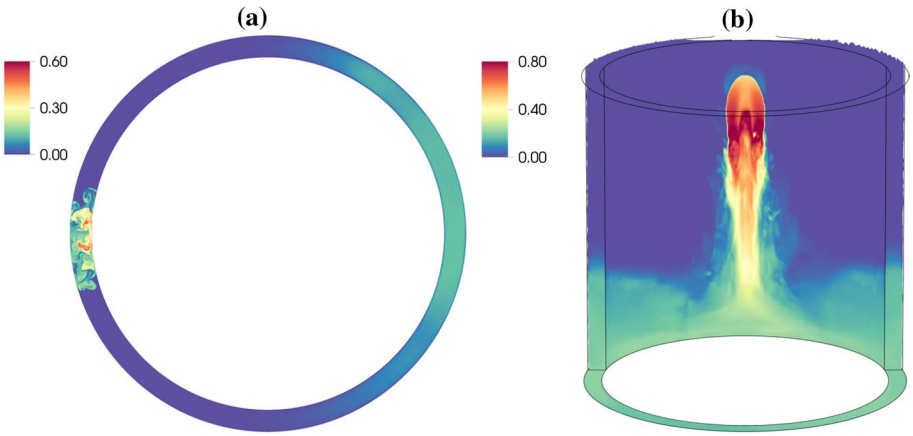

Fig. 17 Instantaneous mass fraction ϕ at $t = 20.84$ s for the simulation VD_4: **a** slice of the downcomer at $y = -17.56$ cm, **b** 3D view of the downcomer inner wall. A related video is available at https://triocfd.cea.fr/databases/CLM_database.

- In the cold leg, the flow is dominated by buoyancy forces rather than turbulent mixing, contrary to the downcomer.
- The effect of mesh change is generally found to be stronger than the effect of the physical model. This observation can be attributed to the low Atwood number, and

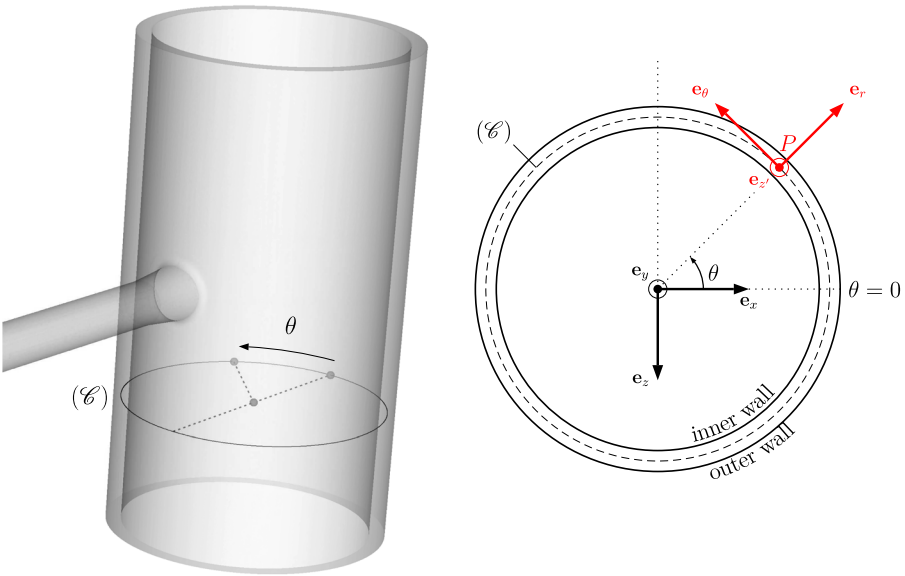

Fig. 18 Definition of a circular profile ($\mathscr{C}$) in the downcomer passing through the middle of the annular gap. This profile is located at the same elevation as the ($\mathscr{L}_{\rm dc}$) line of Fig. 2, *i.e.* $y = -17.56$ cm. At each point P along ($\mathscr{C}$) is attached a cylindrical coordinate system ($\mathbf{e}_r$; $\mathbf{e}_\theta$; $\mathbf{e}_{z'}$). The azimuthal angle θ is such that $\theta = 180°$ is the position of the cold leg opening

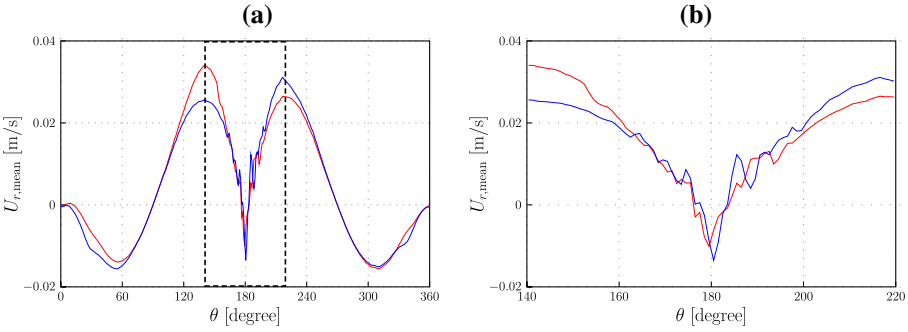

Fig. 19 Plots of the average radial component $U_{r,\rm mean}$ of the velocity in the downcomer along the circular profile ($\mathscr{C}$) represented on Fig. 18, at $t = 20.84$ s: **a** in the range $\theta \in [0° ; 360°]$, **b** zoom on $\theta \in [140° ; 220°]$. The legend is as follows: —— Simulation $\rm BA_4$, —— Simulation $\rm VD_4$

one could expect a larger deviation between the models for an increasing Atwood number.

- Most quantities are found to be reasonably well converged with respect to the mesh, but low-magnitude components would likely require a further mesh refinement. This is expecially true in the downcomer where the strong turbulence constrains to the use of very fine cells in spite of the large amplitude of turbulent scales captured by the finest mesh, as revealed by the power spectra.

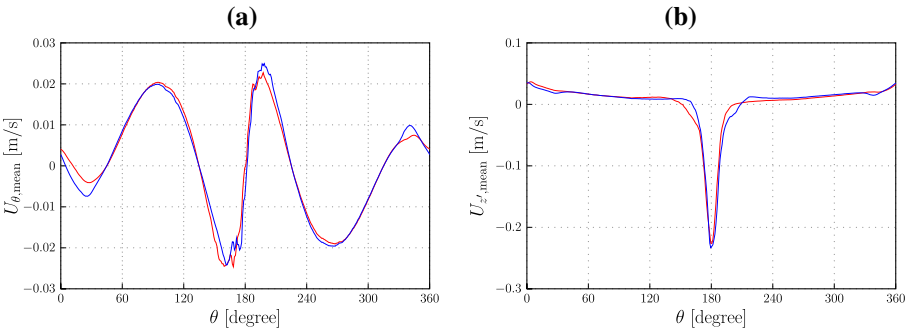

Fig. 20 Plots of the average components of the velocity in the downcomer along the circular profile (𝒞) represented on Fig. 18, at $t = 20.84$ s: **a** azimuthal velocity $U_{\theta,\mathrm{mean}}$, **b** vertical velocity $U_{z',\mathrm{mean}}$. The legend is the same as Fig. 19

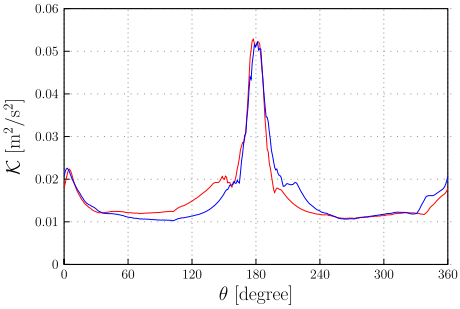

Fig. 21 Plot of the turbulent kinetic energy in the downcomer along the circular profile (𝒞) represented on Fig. 18, at $t = 20.84$ s. The legend is the same as Fig. 19

- The computed solutions appear to be fairly close to the shape and amplitude of PIV profiles in most cases. Thereby, both tested models achieve overall a good agreement with experimental values. In the cold leg, a slightly superior performance of the VD model to the BA model was demonstrated, in terms of accuracy in comparison to experimental data. However, some dubious deviations between LES and experimental measurements were noticed in the downcomer, such as the near-wall behavior of the fall velocity not properly reproduced, and the horizontal velocity poorly predicted.
- Independently of the measured data, the examination of the velocity distribution in the downcomer provides an additional insight into the validation results discussed above. Particularly, the existence of a sharp peak of the horizontal velocity at the cold leg opening leads to a strong uncertainty on its amplitude, and may explain to a large extend the significant difference on U_{mean} between the experiment and simulations, but also between the physical models themselves.
- The experimental data appear to be questionable at some places of the downcomer, with zero values where it would not be expected. There is seemingly no sound experimental data basis for a torough validation of the numerical simulations in the downcomer, or at the very least the experimental data are too incomplete. This encourages caution in the interpretation of the validation results.

Supplementary data are available online at https://triocfd.cea.fr/databases/CLM_database. A video of the mass fraction evolution is provided to complement the understanding of the mixing process. Further investigations of the flow evolution beyond 20.84 s would be necessary for the comprehension of the entire transient phenomenon, as well as additional experimental measurements such as the azimuthal velocity and the mass fraction in the downcomer.

Acknowledgements This work was granted access to the HPC resources of TGCC under the allocation 2019-A0072A10460 attributed by GENCI (Grand Équipement National de Calcul Intensif).

Declarations

Conflict of interest The author declares that he has no conflict of interest.

References

Akbari, S., Taghavi, S.: Injection of a heavy fluid into a light fluid in a closed-end pipe. Phys. Fluids **32**, 063302 (2020)

Akula, B., Ranjan, D.: Dynamics of buoyancy-driven flows at moderately high Atwood numbers. J. Fluid Mech. **795**, 313–355 (2016). https://doi.org/10.1017/jfm.2016.199

Angeli, P.E.: Overview of the TrioCFD code: main features, V&V procedures and typical applications to nuclear engineering. In: 16th International Topical Meeting on Nuclear Reactor Thermalhydraulics. Chicago, USA (2015)

Angeli, P.E.: Verification and validation of LES of a triple parallel jet flow in the context of a thermal striping study. Nucl. Eng. Des. (2019). https://doi.org/10.1016/j.nucengdes.2019.110210

Angeli, P.E., Puscas, A., Fauchet, G., Cartalade, A.: FVCA8 benchmark for the Stokes and Navier–Stokes equations with the TrioCFD code—benchmark session. In: Cancès, C., Omnes, P. (eds.) Finite Volumes for Complex Applications VIII—Methods and Theoretical Aspects, pp. 181–203. Springer (2017)

Aulery, F., Dupuy, D., Toutant, A., Bataille, F., Zhou, Y.: Spectral analysis of turbulence in anisothermal channel flows. Comput. Fluids **151**, 115–131 (2017)

Avellaneda, J., Bataille, F., Toutant, A.: DNS of turbulent low Mach channel flow under asymmetric high temperature gradient: effect of thermal boundary condition on turbulence statistics. Int. J. Heat Fluid Flow **77**, 40–47 (2019). https://doi.org/10.1016/j.ijheatfluidflow.2019.03.002

Benjamin, T.: Gravity currents and related phenomena. J. Fluid Mech. **31**, 209–248 (1968)

Bernard-Michel, G., Saikali, E., Sergent, A., Tenaud, C.: Comparisons of experimental measurements and large eddy simulations for a helium release in a two vents enclosure. Int. J. Hydrog. Energy **44**, 8935–8953 (2019)

Bieder, U., Rodio, M.: Large Eddy Simulation of the injection of cold ECC water into the cold leg of a pressurized water reactor. Nucl. Eng. Des. **341**, 186–197 (2019). https://doi.org/10.1016/j.nucengdes.2018.10.026

Blazek, J.: Computational Fluid Dynamics: Principles and Applications. Elsevier, Amsterdam (2015). https://doi.org/10.1016/C2013-0-19038-1

Calvin, C., Cueto, O., Émonot, P.: An object-oriented approach to the design of fluid mechanics software. ESAIM Math. Model. Numer. Anal. **36**, 907–921 (2002)

Chassaing, P., Antonia, R., Anselmet, F., Joly, L., Sarkar, S.: Variable Density Fluid Turbulence. Springer, Basel (2002). https://doi.org/10.1007/978-94-017-0075-7

Chorin, A.J.: Numerical solution of the Navier–Stokes equations. Math. Comput. **22**, 745–762 (1968)

Chouhan, R., Kansal, A.K., Maheshwari, N., Sharma, A.: Computational studies on pressurized thermal shock in reactor pressure vessel. Ann. Nucl. Energy (2021). https://doi.org/10.1016/j.anucene.2020.107987

Cremer, I., Mutz, A., Trewin, R., Grams, S.: Two-phase pressurized thermal shock analysis with CFD including the effects of free-surface condensation. Nucl. Eng. Des. (2019). https://doi.org/10.1016/j.nucengdes.2019.110282

Crouzeix, M., Raviart, P.A.: Conforming and nonconforming finite element methods for solving the stationary Stokes equations I. ESAIM Math. Model. Numer. Anal. **7**, 33–75 (1973)
Ducros, F., Bieder, U., Cioni, O., Fortin, T., Fournier, B., Fauchet, G., Quéméré, P.: Verification and validation considerations regarding the qualification of numerical schemes for LES for dilution problems. Nucl. Eng. Des. **240**, 2123–2130 (2010)
Dupuy, D., Toutant, A., Bataille, F.: Turbulence kinetic energy exchanges in flows with highly variable fluid properties. J. Fluid Mech. **834**, 5–54 (2018). https://doi.org/10.1017/jfm.2017.729
Dupuy, D., Toutant, A., Bataille, F.: Effect of the Reynolds number on turbulence kinetic energy exchanges in flows with highly variable fluid properties. Phys. Fluids **31**, 015104 (2019). https://doi.org/10.1063/1.5080769
Elmo, M., Cioni, O.: Low Mach number model for compressible flows and application to HTR. Nucl. Eng. Des. **222**, 117–124 (2003)
Eltayeb, A., Tan, S., Ala, A., Zhang, Q.: The study of the influence of slug density on the mixing performance in the reactor vessel, using PLIF experiment and FLUENT simulation. Prog. Nucl. Energy (2021). https://doi.org/10.1016/j.pnucene.2020.103558
Émonot, P.: Méthodes de volumes éléments finis : applications aux équations de Navier-Stokes et résultats de convergence. Ph.D. thesis, Université Claude Bernard – Lyon I (1992)
Fortin, T.: Une méthode d'éléments finis à décomposition L2 d'ordre élevé motivée par la simulation des écoulements diphasiques bas Mach. Ph.D. thesis, Université Paris VI (2006)
Garnier, E., Adams, N., Sagaut, P.: Large Eddy Simulation for Compressible Flows. Springer, Basel (2009). https://doi.org/10.1007/978-90-481-2819-8
Hasnain, A., Segura, E., Alba, K.: Buoyant displacement flow of immiscible fluids in inclined pipes. J. Fluid Mech. **824**, 661–687 (2017). https://doi.org/10.1017/jfm.2017.367
Hassan, M., Xiong, J., Cheng, X.: Unsteady RANS simulation of OECD-TAMU cold-leg mixing benchmark. Nucl. Eng. Des. (2021). https://doi.org/10.1016/j.nucengdes.2020.110978
Heib, S.: Nouvelles discrétisations non structurées pour les écoulements de fluides à incompressibilité renforcée. Ph.D. thesis, Université Pierre et Marie Curie (2003)
Herranz, L., Jacquemain, D., Nitheanandan, T., Sandberg, N., Barré, F., Bechta, S., Choi, K.Y., D'Auria, F., Lee, R., Nakamura, H.: The working group on the analysis and management of accidents (WGAMA): a historical review of major contributions. Prog. Nucl. Energy (2020). https://doi.org/10.1016/j.pnucene.2020.103432
Höhne, T., Kliem, S., Bieder, U.: IAEA CRP benchmark of ROCOM PTS test case for the use of CFD in reactor design using the CFD-Codes ANSYS CFX and TrioCFD. Nucl. Eng. Des. **333**, 161–180 (2018). https://doi.org/10.1016/j.nucengdes.2018.04.017
Hu, P., Chen, G., Tian, Z., Kang, H., Jin, Y., Appah, T.: Investigating on multi-RANS models coupling simulation for flow mixing experiments. Ann. Nucl. Energy (2020). https://doi.org/10.1016/j.anucene.2020.107389
Huang, M., Höhne, T.: Numerical simulation of multicomponent flows with the presence of density gradients for the upgrading of advanced turbulence models. Nucl. Eng. Des. **344**, 28–37 (2019)
Kumara, G.V., Kampili, M., Kelm, S., Prakasha, K.A., Allelein, H.J.: CFD modelling of buoyancy driven flows in enclosures with relevance to nuclear reactor safety. Nucl. Eng. Des. (2020). https://doi.org/10.1016/j.nucengdes.2020.110682
Kuzmin, D., Turek, S.: High-resolution FEM-TVD schemes based on a fully multidimensional flux limiter. J. Comput. Phys. **198**, 131–158 (2004)
Lai, J., Merzari, E., Hassan, Y.: Sensitivity analyses in a buoyancy-driven closed system with high resolution CFD using Boussinesq approximation and variable density models. Int. J. Heat Fluid Flow **75**, 1–13 (2019)
Lai, J., Merzari, E., Hassan, Y., Fischer, P., Marin, O.: Verification and validation of large eddy simulation with Nek5000 for cold leg mixing benchmark. Nucl. Eng. Des. (2020). https://doi.org/10.1016/j.nucengdes.2019.110427
Lefauve, A., Linden, P.: Buoyancy-driven exchange flows in inclined ducts. J. Fluid Mech. (2020). https://doi.org/10.1017/jfm.2020.212
Li, J., Wang, M., Fang, D., Wang, J., Liu, D., Tian, W., Qiu, S., Su, G.: CFD simulation on the transient process of coolant mixing phenomenon in reactor pressure vessel. Ann. Nucl. Energy (2021). https://doi.org/10.1016/j.anucene.2020.108045
Macpherson, G., Tunstall, R.: CFD validation of buoyancy driven jet spreading, mixing and wall interaction. Nucl. Eng. Des. (2020). https://doi.org/10.1016/j.nucengdes.2020.110703
Meyers, J., Geurts, B., Sagaut, P.: Quality and Reliability of Large-Eddy Simulations. Springer, Basel (2008). https://doi.org/10.1007/978-1-4020-8578-9

Nicoud, F., Ducros, F.: Subgrid-scale stress modelling based on the square of the velocity gradient tensor. Flow Turbul. Combust. **62**, 183–200 (1999)

Orea, D., Vaghetto, R., Nguyen, T., Hassan, Y.: Experimental measurements of flow mixing in cold leg of a pressurized water reactor. Ann. Nucl. Energy (2020). https://doi.org/10.1016/j.anucene.2019.107137

Rakhimov, A.C., Visser, D., Komen, E.: Uncertainty quantification method for CFD applied to the turbulent mixing of two water layers. Nucl. Eng. Des. **333**, 1–15 (2018). https://doi.org/10.1016/j.nucengdes.2018.04.004

Ramaprabhu, P., Andrews, M.J.: Simultaneous measurements of velocity and density in buoyancy-driven mixing. Exp. Fluids **34**, 98–106 (2003). https://doi.org/10.1007/s00348-002-0538-0

Ruan, X., Morishita, K.: Pressurized thermal shock analysis of a reactor pressure vessel for optimizing the maintenance strategy: effect of asymmetric reactor cooling. Nucl. Eng. Des. (2021). https://doi.org/10.1016/j.nucengdes.2020.111021

Saikali, E., Bernard-Michel, G., Sergent, A., Tenaud, C., Salem, R.: Highly resolved large eddy simulations of a binary mixture flow in a cavity with two vents: influence of the computational domain. Int. J. Hydrog. Energy **44**, 8856–8873 (2019)

Shams, A., Santis, D.D., Rosa, D., Kwiatkowski, T., Komen, E.: Direct numerical simulation of flow and heat transfer in a simplified pressurized thermal shock scenario. Int. J. Heat Mass Transf. **135**, 517–540 (2019)

Taghavi, S., Alba, K., Frigaard, I.: Buoyant miscible displacement flows at moderate viscosity ratios and low Atwood numbers in near-horizontal ducts. Chem. Eng. Sci. **69**, 404–418 (2012a). https://doi.org/10.1016/j.ces.2011.10.065

Taghavi, S., Alba, K., Seon, T., Wielage-Burchard, K., Martinez, D., Frigaard, I.: Miscible displacement flows in near-horizontal ducts at low Atwood number. J. Fluid Mech. **696**, 175–214 (2012b). https://doi.org/10.1017/jfm.2012.26

Temam, R.: Une méthode d'approximation de la solution des équations de Navier–Stokes. Bull. Soc. Math. France **96**, 115–152 (1968)

Thamaraiselvi, K., Vishnuvardhan, S.: Fracture studies on reactor pressure vessel subjected to pressurised thermal shock: a review. Nucl. Eng. Des. (2020). https://doi.org/10.1016/j.nucengdes.2019.110471

Uitslag-Doolaard, H., Stefanini, L., Shams, A., Blom, F.: Numerical prediction of a single phase Pressurized Thermal Shock scenario for crack assessment in an Reactor Pressure Vessel wall. Ann. Nucl. Energy (2020). https://doi.org/10.1016/j.anucene.2020.107563

Vreman, B., Geurts, B., Kuerten, H.: A priori tests of large eddy simulation of the compressible plane mixing layer. J. Eng. Math. **29**, 299–327 (1995)

Vreman, B., Geurts, B., Kuerten, H.: Large-eddy simulation of the turbulent mixing layer. J. Fluid Mech. **339**, 357–390 (1997)